



The formation of Qulong adakites and their relationship with porphyry copper deposit: Geochemical constraints



Yong-bin Hu ^{a,b}, Ji-qiang Liu ^{a,c}, Ming-xing Ling ^d, Wei Ding ^a, Yan Liu ^e, Robert E. Zartman ^a, Xiu-feng Ma ^a, Dun-qi Liu ^e, Chan-chan Zhang ^{a,b}, Sai-jun Sun ^{a,b}, Li-peng Zhang ^{a,b}, Kai Wu ^{a,b}, Wei-dong Sun ^{a,f,*}

^a CAS Key Laboratory of Mineralogy and Metallogeny, Guangzhou Institute of Geochemistry, Chinese Academy of Sciences, Guangzhou 510640, China

^b University of Chinese Academy of Sciences, Beijing 10094, China

^c SOA Key Laboratory of Submarine Geoscience, Second Institute of Oceanography, State Oceanic Administration, Hangzhou 310012, China

^d State Key Laboratory of Isotope Geochemistry, Guangzhou Institute of Geochemistry, Chinese Academy of Sciences, Guangzhou 510640, China

^e Institute of Geology, Chinese Academy of Geological Sciences, Beijing, China

^f CAS Center for Excellence in Tibetan Plateau Earth Sciences, Chinese Academy of Sciences, Beijing 100101 China

ARTICLE INFO

Article history:

Received 4 June 2014

Accepted 26 December 2014

Available online 14 February 2015

Keywords:

Porphyry Cu deposit

Adakite

Zircon Hf-O isotopes

Qulong

Gangdese

ABSTRACT

Qulong porphyry Cu deposit is the largest Cu deposit in China so far discovered, with total reserves of 10.6 Mt Cu@0.5% and 0.5 Mt Mo@0.03%. The petrogenesis of the Miocene intrusion and its genetic association with Cu mineralization have been debated. This study presents new results on whole rock major and trace elements, Sr-Nd isotopes, zircon U-Pb dating, Hf-O isotopic compositions of the Qulong ore-bearing and barren adakites. All the Qulong adakites studied here have low MgO (<2 wt.%), high K₂O (between 2 wt.% and 6 wt.%), with K₂O/Na₂O ratios ranging from 0.2–2.0. The SiO₂ contents are mostly higher than 64 wt.%. These are dramatically different from ore-forming adakites in the circum-Pacific region and other places in general. Ore-bearing adakites have systematically higher SiO₂ and K₂O compared with barren ones, likely due to the addition of Si and K during alteration and mineralization. Magmatic zircons from these two series of intrusions have U-Pb ages of 16.6 ± 0.5–17.0 ± 0.6 Ma and 16.7 ± 0.3–17.4 ± 0.4 Ma, respectively, which are identical to each other within analytical errors but are systematically older than although marginally overlap with the Re-Os isochron ages of 15.36 ± 0.21–16.41 ± 0.48 Ma. The Qulong porphyries have geochemical characteristics of typical adakites, with Sr = 259–1195 ppm, Y = 1.91–9.12 ppm, Yb = 0.2–0.92 ppm, Sr/Y = 49–202 ppm, and (La/Yb)_n = 13–49 for both ore-bearing and barren adakites. In a Sr/Y versus (La/Yb)_n diagram, most of the samples plot in the low part of circum-Pacific field, close to the field defined by Dabie adakites. Some of the ore-bearing adakites even plot in the Dabie adakite field, indicating that both slab melts and lower continental crust melts have been involved. Zircons from the ore-bearing adakites have δ¹⁸O ranging from 5.1 to 7.3‰ (average 6.4‰) and εHf(t) from 1.9 to 10.4‰, which plot close to MORB. Similarly, zircons from the barren adakite have δ¹⁸O ranging from 4.0 to 7.4‰ (average 6.3‰) and εHf(t) from 5.6 to 9.3‰, mostly plotting close to MORB values, too. In-situ zircon Hf-O isotopic measurements for the most samples yield a binary mixing trend between mantle- and crustal-derived melts, with mantle-related sources as the main contributor. Whole-rock Sr-Nd isotopes also show small variations, with (⁸⁷Sr/⁸⁶Sr)_i = 0.704904–0.705053 and εNd(t) = -0.04–0.61. The dramatic differences between Qulong and circum-Pacific adakites suggest that either Qulong porphyry Cu deposit is unique, or the ore-bearing adakites are not the ore-forming porphyry. Considering the identical geochemical characteristics of the ore-bearing and barren adakites, the textures (some samples are not porphyry) and the systematically older ages compared to Re-Os isochron ages, the latter is preferred. In contrast to earlier adakitic granites, recently studied porphyries in the central phase of the Qulong deposit have zircon U-Pb ages identical to the Re-Os ages, and thus are more likely to be the ore-forming porphyry. All these suggest that slab melting rather than partial melting of Gangdese arc materials is responsible to the Qulong porphyry Cu deposit.

© 2015 Elsevier B.V. All rights reserved.

1. Introduction

Numerous studies have been carried out on Miocene (26–10 Ma) adakitic porphyries in the Gangdese belt (Chung et al., 2003, 2009; Gao et al., 2003b, 2007b, 2010b; Guo et al., 2007; Hou et al., 2003,

* Corresponding author at: CAS Key Laboratory of Mineralogy and Metallogeny, Guangzhou Institute of Geochemistry, Chinese Academy of Sciences, Guangzhou 510640, China.

E-mail address: weidongsun@gig.ac.cn (W. Sun).

2004b; Qu et al., 2004, 2007; Xu et al., 2010). These adakites extend roughly east-westward along the Gangdese belt, to the north of the Yarlung Tsangpo suture zone in southern Tibetan Plateau (Meng et al., 2003b; Zheng et al., 2004). It is the largest Cu–Mo mineralization belt in China.

Porphyry Cu (Au) deposits are one of the most important economic mineral associations (Cooke et al., 2005; Sillitoe, 2010; Sun et al., 2013, 2015), mostly distributed along convergent margins, such as the circum-Pacific belt and the Tethys belt (Cooke et al., 2005; Qu et al., 2001; Sillitoe, 1997; Sun et al., 2010, 2011, 2012b). Considering that porphyry Cu deposits are usually closely associated with adakites (Ling et al., 2009, 2011, 2013b; Oyarzun et al., 2001; Sun et al., 2011, 2013), it is very important to study the origin and relationship of adakites with the Gangdese porphyry copper deposits.

Various models have been proposed for the petrogenesis of these adakites (Chung et al., 2003; Gao et al., 2003b, 2007b; Guo et al., 2007; Hou et al., 2004b; Li et al., 2011; Qu et al., 2004, 2007; Xu et al., 2010), including: (1) partial melting of the subducted Neotethyan oceanic crust (Gao et al., 2003b; Hou et al., 2003, 2004b; Qu et al., 2004); (2) partial melting of the thickened Lhasa mafic lower crust (Chung et al., 2003, 2005; Guo et al., 2007; Li et al., 2011); (3) partial melting of an upper mantle source metasomatized by slab-derived melts (Gao et al., 2007b); (4) partial melting of the subducted Indian continental crust beneath the southern Lhasa terrane (Xu et al., 2010).

The debate is partial because Qulong and also other adakites that host porphyry deposits suffered pervasive hydrothermal alteration that has modified their primary textural and chemical characteristics (Xiao et al., 2012a; Yang et al., 2009; Zheng et al., 2004). Zircon is an accessory mineral commonly found in intermediate-acid magmatic rocks, and it is highly resistant to disturbance by hydrothermal alteration and weathering, which can preserve information on magma composition and thus is an excellent tool to trace the magma source through trace element and isotope information (Watson and Cherniak, 1997).

In this paper, we analyze the trace elements and in-situ U–Pb and Hf–O isotopes in zircon from ore-bearing and barren adakites from the Qulong deposit. Combined with whole rock geochemistry, Sr–Nd isotopes, zircon U–Pb ages, trace elements and Hf–O isotope compositions were studied, aiming at better constraints on the formation of these adakites and their association with the porphyry mineralization.

2. Geological background and sample descriptions

2.1. Regional geology

The Tibet plateau, the largest plateau on Earth, is part of the Alps–Himalayan orogenic belt (Allegre et al., 1984; Chung et al., 1998, 2005; Yin and Harrison, 2000), formed due to the continental collision and subduction of India underneath Eurasia (Allegre et al., 1984; Chung et al., 2012; Yin and Harrison, 2000). It is mainly composed of four blocks, which, from north to south, include: the Songpan–Ganzi flysch complex belt, the Qiangtang block, the Lhasa terrane and the Himalayas (Yin and Harrison, 2000; Fig. 1A). The Qiangtang and Lhasa blocks, which constitute the main body of the Tibet plateau, were derived from the northern margin of Gondwana continent, and its evolution history involves a series of plate tectonic processes, i.e., break-up, drift, and attachment of the Paleozoic and Mesozoic micro-blocks to the southern margin of the Asian continent (Audley-Charles et al., 1988; Yin and Harrison, 2000; Zhu et al., 2011). The Qiangtang block is bounded to the northwest by the Tarim block, and to the northeast by the Songpan–Ganzi mixtite belt and the Yangtze block. The Lhasa terrane, located between the Bangonghu–Nujiang suture zone and the Yarlung Tsangpo suture zone of the Late Jurassic and the Early Cretaceous, is a huge tectonic-magmatic belt (Chang and Zhang, 1973) with large Cretaceous and Cenozoic batholiths. The Lhasa terrane in the southern Tibetan Plateau is divided into northern, central, and southern subterranea (Fig. 1A),

separated by the Shiquan River–Nam Tso Mélange Zone and the Luobadui–Milashan Fault (Pan et al., 2006; Zhu et al., 2012b).

In southern Tibet, the Lhasa terrane consists mainly of the Gangdese orogenic belt, which was resulted from the northward subduction of the Neo-Tethyan oceanic lithosphere beneath Asia and the subsequent India–Asia collision (Yin and Harrison, 2000). The Gangdese orogenic belt is composed mainly of Late Paleocene–Early Eocene (60–40 Ma) Linzizong Formation volcanic rocks and Cretaceous–Tertiary (120–24 Ma) granite batholiths (Allegre et al., 1984; Mo et al., 2008). According to previous studies, multiple metallogenic events occurred in the different tectonic settings of the Indo-Asian collision, identified as the main-collisional convergent setting (~65–41 Ma), the late-collisional transform setting (~40–26 Ma), and the post-collisional crustal extension setting (~25–0 Ma) (Chung et al., 2005; Hou et al., 2006). The Cenozoic porphyries were emplaced into the same terrane occupied by the older Gangdese granite batholiths, creating a narrow porphyry copper metallogenic belt north of and along the Yarlung Tsangpo suture zone. Contained within this metallogenic belt are scores of Cenozoic porphyry Cu (Mo) deposits and smaller ore occurrences.

With several ore deposits, i.e., Qulong, Jiama, Chongjiang, Tinggong, Bangpu and Zhunuo et al., discovered in recent years, south Gangdese has become a huge porphyry Cu–Au–Mo deposit belt, and has the potential of becoming the largest Cu–Au–Mo resource in China (Qu et al., 2001). These deposits are of Cenozoic age, with most significant porphyry Cu–Mo ore bodies forming in the Miocene (14–17 Ma) (Meng et al., 2003a, 2004; Rui et al., 2003; Wang et al., 2012; Ying et al., 2010).

The Qulong porphyry copper deposit, located in the east part of the Gangdese belt (latitude 29°36'–29°40' N, longitude 91°33'–91°37' E), about 50 km east of Lhasa city (Fig. 1A), was found by the Regional Geological Team of the Tibetan Geological Survey. By 2009, Qulong porphyry deposit, with reserves of 10.6 Mt Cu@0.5% and 0.5 Mt Mo@0.03% (Xiao et al., 2012a), together with the adjacent Jiama porphyry-skarn deposit, had become the largest porphyry-skarn type copper mining area in China.

2.2. Geology of the deposit

The Qulong deposit is hosted in the Jurassic Yeba Formation. Three recognizable nearly east–west-trending lithologic units of the Jurassic Yeba Formation, with an age of 174.4 Ma (Dong et al., 2006), were present in the Qulong district (Fig. 1B): (1) A basal member, consisting of andesitic crystal tuff and ignimbrite with intense hornfels, contacts metamorphism mainly in the south-central part of the district. (2) A middle member, comprising medium to thin limestone and laminated slate with propylitization metamorphism, is found largely to the north of the deposit. (3) An upper member consisting of sericitic slate, tuff and small amounts of rhyolite, is distributed throughout the mapped area. For more details, please refer to Yang et al. (2009).

The magmatic rocks are of Jurassic and Miocene ages and include: (1) Middle Jurassic ductilely deformed granite porphyry, (2) Miocene granodiorite–adamellite, (3) Miocene monzogranite porphyry related to the two main stages of mineralization, and (4) diorite porphyry associated with a late stage of mineralization (Fig. 1B).

2.2.1. Magmatic rocks

2.2.1.1. Jurassic intrusive rocks. Mineralization in the Jurassic porphyries, characterized by abundant pyrite veins and quartz–sericite alteration with local minor epidote alteration, tends to be fracture controlled. Sulfide mineral-bearing veins are typically planar and composed primarily of quartz and pyrite at all exposed levels with sericite alteration selvages. The whole rock chemical analyses of the porphyry show that the rock contains about 74% to 82% SiO₂, 3.3% to 6.5% K₂O and 2.4% to 4.3% Na₂O, and thus belongs to high-K calc-alkaline series (Yang et al.,

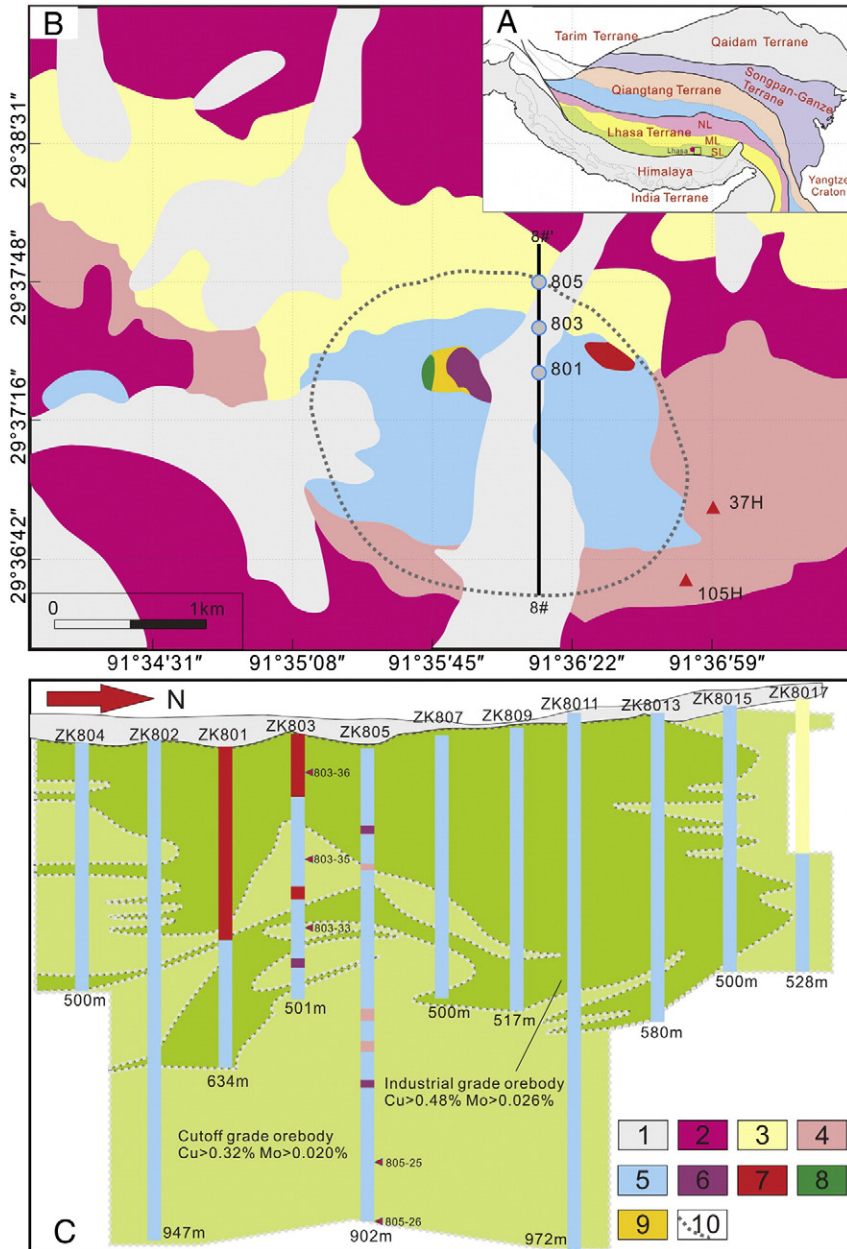


Fig. 1. (A) Tectonic outline of the Tibetan Plateau showing the subdivision of the Lhasa Terrane. NL = Northern Lhasa subterrane; CL = Central Lhasa subterrane; SL = Southern Lhasa subterrane. (B) Geology sketch map of the Qulong porphyry Cu deposit modified after Tibet Julong Copper Co., Ltd. (2008) and Xiao et al. (2012b). 1: Quaternary sediments; 2: Jurassic tuff; 3: Jurassic rhyolite porphyry; 4: Miocene granodiorite; 5: Miocene biotite monozonite; 6: Miocene monozonite porphyry; 7: Miocene diorite porphyry; 8: Miocene granodiorite porphyry; 9: Breccia; 10: Orebody boundary. (C) Cross-section (8#) of the Qulong porphyry copper deposit, Tibet. Also shown are sample locations.

2008a). Zircons from one porphyry sample were dated by SHRIMP and yielded an age of 182.3 Ma (Yang et al., 2008a).

As shown in Fig. 1B, Jurassic rhyolitic porphyries are situated in the middle-north part of the deposit, which intruded the Yeba Formation volcanic rocks and have nothing to do with porphyry Cu-mineralization (Yang et al., 2008a; Zheng et al., 2004). They are characterized predominately by felsic minerals together with a minor amount of dark minerals. Quartz and K-feldspar are the main phenocryst minerals. The matrix of the porphyries has a mineralogy similar to that of the phenocrysts, and consists mainly of quartz with minor feldspar and biotite. Accessory minerals include zircon, apatite, sphene, and magnetite. Quartz phenocrysts are irregular and anhedral in shape, mostly consisting of aggregates of several small quartz crystals.

K-feldspar phenocrysts are subhedral, commonly displaying quartz-sericite and clay alteration. The porphyries in field outcrop are strongly weathered and dominated by phyllitic alteration, local epidotization, minor pyritization and chalcopyritization. The Jurassic rhyolitic porphyries define a phyllitic alteration belt encompassing the whole porphyry bordering. The 182.3 Ma zircon age (Yang et al., 2011) of the porphyry makes it appreciably older than the Miocene ore-bearing rock, and thus allows it no role in the formation of the ore deposit except as a wall rock of the ore body.

2.2.1.2. Miocene intrusive rocks. Among Miocene intrusive rocks, the granodiorite intrudes the Jurassic rhyolitic porphyry and Yeba Formation tuff as well as delineates the southern and eastern margins of

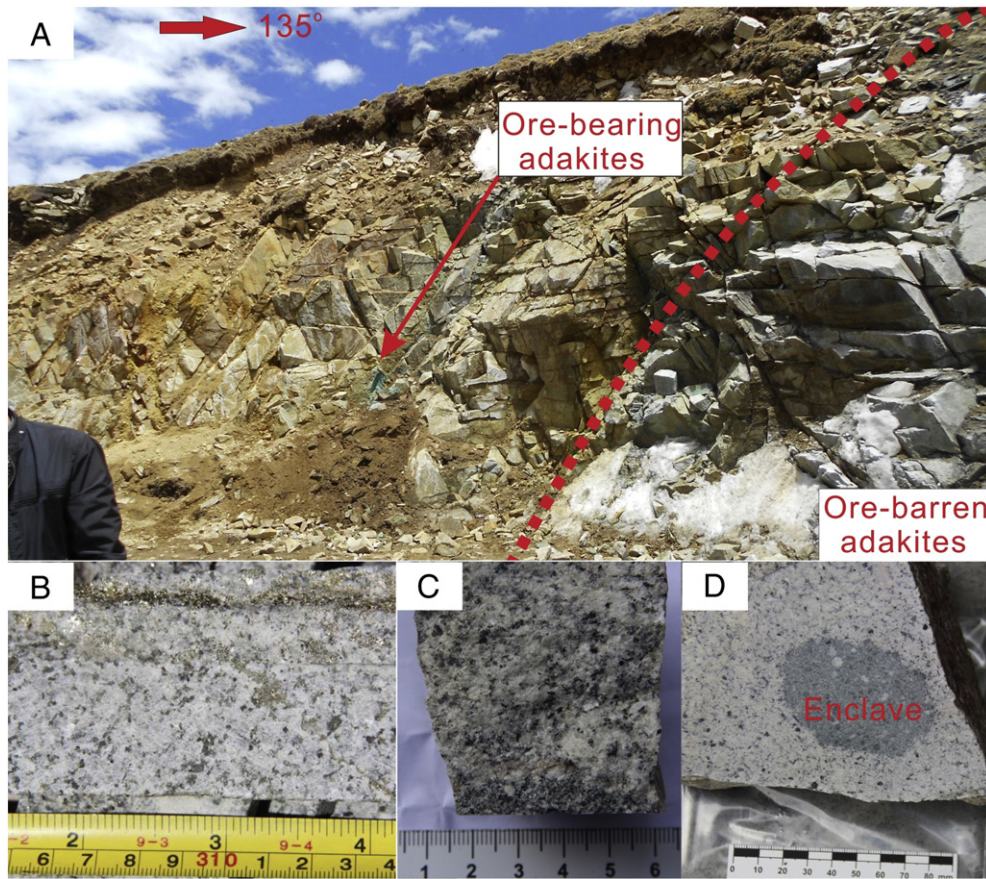


Fig. 2. (A) Picture of Qulong ore-bearing and barren adakitic intrusion, showing the boundary of ore-bearing adakite (monozonite) and barren adakite (granodiorite). (B) Ore-bearing adakite; (C) Barren adakite; (D) Barren adakite and enclave in it.

the ore body, with an outcrop area of $>5 \text{ km}^2$ (Figs. 1B, 2). The main mineral assemblage of this rock is medium to coarse grained plagioclase, K-feldspar, quartz and small amounts of amphibole and biotite. Accessory minerals are zircon, apatite, magnetite and titanite (Xiao et al., 2012a; Yang et al., 2009; Zheng et al., 2004).

The biotite monzogranite intrudes the granodiorite and crops out in an area of 4 km^2 in the central part of the ore district, where it is cross cut by many thin diabase and diorite dykes (Figs. 1B, 2) (Yang et al., 2009; Zheng et al., 2004). The mineral assemblage of this rock is composed of plagioclase, K-feldspar, quartz and a minor amount of biotites in an aphanitic groundmass of quartz and plagioclase. Accessory minerals are zircon, apatite, magnetite, rutile and titanite. The biotite monzogranite contains more biotite and quartz than the granodiorite but without amphibole.

The monzogranite porphyry (Fig. 1B) intruded near the center part of the biotite monzogranite body, with an outcrop area of about 0.5 km^2 (Gao and Zheng, 2006). A distinctive crypto-explosive breccia crops out at its western margin (Zheng et al., 2004). The monzogranite porphyry displays a typical porphyritic texture, with a mineral assemblage of quartz, plagioclase and K-feldspar in an aphanitic groundmass of quartz, plagioclase, K-feldspar and minor biotites. Accessory minerals are apatite, zircon, magnetite, rutile and titanite. The monzogranite porphyry underwent alteration manifested by lots of secondary sericite, biotite and K-feldspar.

The granodiorite porphyry (Fig. 1B) occurs in small dyke bodies intruded into the west part of the biotite monzogranite with an outcrop area of 0.4 km^2 (Zheng et al., 2004). The mineral assemblage of this rock is plagioclase, K-feldspar, quartz and biotite phenocrysts in an

aphanitic groundmass of quartz, plagioclase, K-feldspar and biotite. Accessory minerals are apatite, zircon, and magnetite.

The diorite porphyry occurs as a dyke intruded at the northeast margin of the biotite monzogranite (Fig. 1B) (Qin et al., 2014). The mineral assemblage of this rock is plagioclase, K-feldspar, quartz and amphibole phenocrysts in an aphanitic groundmass of plagioclase and amphibole. Accessory minerals are apatite, zircon, titanite and magnetite.

2.2.2. Alteration and mineralization

Large-scale (with an area of $>20 \text{ km}^2$) hydrothermal alteration is observed in the Qulong ore district. Almost every type of rock in the Qulong ore district is affected by hydrothermal alteration. The alteration zones display typical concentric alteration, comprised in the chronological order of alteration, of a potassic zone, sericitic zone, propylitic zone and argillic zone (Qin et al., 2014), which emanate from the ore-bearing porphyry center, i.e. the monzogranite porphyry and granodiorite porphyry, outward and upward. Moreover, the early stage alteration zones are progressively overprinted by later alteration. The highest temperature alteration zone reached at a locality correlates well with the mineralization type it hosts (Qin et al., 2014; Yang et al., 2009; Zheng et al., 2004).

Potassic alteration assemblages with secondary K-feldspar and biotite dominate in the deep part of the monzogranite porphyry and granodiorite porphyry and constitute the porphyry Cu ore body. The potassic alteration zone in these porphyries is characterized by pervasive occurrences of sericite, magnetite, sodium feldspar, anhydrite and carbonate minerals. Secondary biotite and thin, siliceous vein are also widespread.

Albite reaction rim on the plagioclase often occurs as a result of Na precipitation during the process of K-feldspar metasomatism. K-feldspar alteration are mainly veinlet and porphyritic. Potassic alteration is often superimposed on argillic and carbonation alteration appears gray and white in hand specimen. The purple and crumbly anhydrite vein intergrowths are associated with secondary biotite, quartz and magnetite, and contain many inclusions. The ore mineral assemblages occur disseminated throughout the porphyries and as chalcopyrite–pyrite–molybdenite net veins (Qin et al., 2014; Yang et al., 2009; Zheng et al., 2004).

The sericite–quartz alteration zone is located at the outer edge of the ore-bearing porphyry and into the peripheral biotite monzogranite, surrounding and overlaying the potassic alteration zone. The alteration assemblages consist predominately of sericite, quartz and locally chlorite and minor fluorite. K-feldspar and plagioclase suffered varying degrees of sericitization. Quartz phenocrysts have frequently developed secondary overgrowths. Overall, the mineralization of this zone is widespread but relatively weak. The ore mineral assemblages in this alteration zone occur in thin, disseminated veins, and as chalcopyrite–pyrite–bornite net veins, and chalcopyrite–galena–sphalerite and molybdenite quartz veinlet (Qin et al., 2014; Yang et al., 2009; Zheng et al., 2004).

The propylitic alteration zone is weakly developed in the porphyries and occurs mainly in the granodiorite, Jurassic rhyolite porphyry, and Yeba Formation tuff. The most common alteration of the granodiorite minerals is to chlorite, epidote and carbonate. Chlorite and epidote replace the biotite phenocrysts along their rim, cleavage, and at their centers, while the pseudomorphs of biotite are occasionally retained. The alteration minerals in the Yeba Formation are epidote and minor chlorite, which usually occurs along the rim and cleavage of amphibole and biotite. The ore minerals occur in fine veins and as disseminated pyrite, chalcopyrite and magnetite (Qin et al., 2014; Yang et al., 2009; Zheng et al., 2004).

The argillic alteration zone is weakly developed, located at and overlapping onto the transitional zone from potassic alteration zone to sericite–quartz alteration zone. It is especially developed in the shallow, tectonic fracture and fault zone, but becomes weaker at depth. The argillic alteration zone is characterized by quartz, kaolinite and other clay minerals. The main metal mineral assemblage is disseminated chalcopyrite–pyrite–covellite–malachite–chalcocite–molybdenite (Qin et al., 2014; Yang et al., 2009; Zheng et al., 2004).

The largest Gangdese ore bodies are mainly located in the potassic alteration zone and the transitional zone from potassic alteration to sericite–quartz alteration, having disseminated, vein, and net vein copper mineralization. Their wall-rocks are monzogranite porphyry, granodiorite porphyry and biotite monzogranite, having no direct contact with the Jurassic rhyolite porphyry. The sulfides are mainly pyrite, chalcopyrite, molybdenite and minor bornite, chalcocite and very small amounts of sphalerite and galena. Pyrite is mainly euhedral to subhedral, and chalcopyrite is anhedral-grained. Rutile and magnetite

are anhedral-grained, but rutiles from the exsolution of biotite are needles. Molybdenite possesses its characteristic flexibility, blade shape, and greasy luster occasionally occurring in clusters, which are located in quartz–molybdenite veins and cut across the early stage chalcopyrite + pyrite veins. Locally disseminated molybdenite can be observed. The most common gangue minerals are quartz, biotite, sericite, K-feldspar, plagioclase and clay minerals.

2.3. Sample descriptions and preparations

Four ore-bearing samples and two barren samples were selected for the zircon U–Pb dating, Hf–O isotope and trace element analyses. Sample 805-25 is from drillhole ZK805 at a depth of 95.2 m; 2009-37 is from ZK2009 at a depth of 390 m; samples 803-33 and 803-35 are from drillhole ZK803 at depths of 380.9 m and 259 m respectively (Fig. 1C); and sample 2009-37 is from drillhole ZK2009 at a depth of 390 m; barren samples contain 4406-1 and 4406-2 (from drillhole ZK4406 at depths of 259 m and 335 m respectively), and QL37H and QL105H from the barren granodiorite intrusion (Fig. 1B).

Zircon grains were first separated through powdering samples to about 40–60 mesh, desliming in water, followed by standard heavy liquid and magnetic separation. The zircons then were hand-picked under a binocular microscope and mounted on double-sided sticky tape prior to casting in an epoxy mount and polished down to near half sections to expose internal structures. Optical microscopy images and cathodoluminescent were taken in CAS Key Laboratory of Mineralogy and Metallogeny, Guangzhou Institute of Geochemistry, Chinese Academy of Sciences in order to avoid tiny melt, fluid and apatite inclusions commonly captured in zircons during in-situ analyses prior to U–Th–Pb and Hf–O isotope analysis.

3. Analytical methods

3.1. Major and trace element geochemistry

The major and trace element analysis for the bulk rock samples was mainly carried out in the State Key Laboratory of Isotope Geochemistry, Guangzhou Institute of Geochemistry, Chinese Academy of Sciences. And major and trace elements of the samples with superscript ‘a’ and major elements of the samples with superscript ‘c’ for high sulfur were analyzed in the ALS Chemex (Guangzhou) Co., Ltd. (through ICP-AES and ICP-MS, refer to notes of Table 2). The following are the analytical methods of major and trace element analysis carried out in the GIG.

Fresh samples were first broken to centimeter sizes; only the fresh pieces were selected, washed with deionized water, dried and then ground to less than 200 mesh (0.5200 ± 0.0001 g) for geochemical analyses. Sample powders were fluxed with $\text{Li}_2\text{B}_4\text{O}_7$ (1:8) to make homogeneous glass disks at 1250 °C using a V8C automatic fusion machine produced by the Analymate Company in China. The bulk rock major

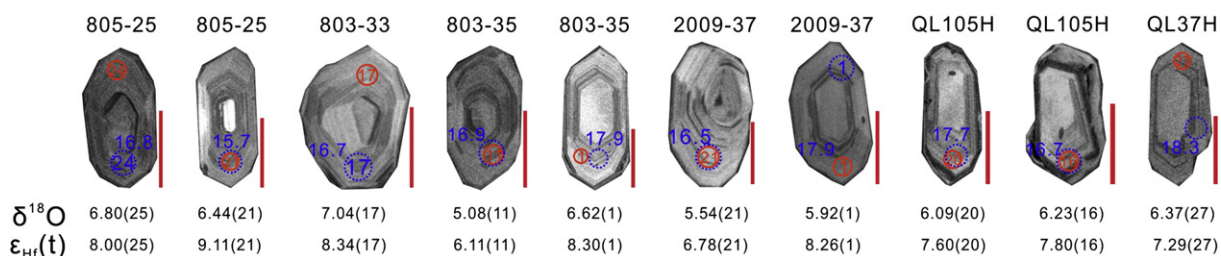


Fig. 3. Representative cathodoluminescence (CL) images of zircons analyzed in-situ for U–Pb, Hf and O isotopes from Qulong adakites. Dotted blue circles indicate the LA-ICP-MS analysis spots for U–Pb, and the red solid circles denote the LA-MC-ICP-MS analysis spots for Hf isotopes and the SHRIMP analysis spots for O isotopes. Numbers near the analysis dotted circle are the U–Pb ages, in Ma. The red scale bars are 100 μm long.

elements were analyzed using X-ray fluorescence spectrometry techniques (Rigaku 100e). The analytical errors for major elements were better than 1%.

For trace element analysis, sample powders were first dissolved using distilled HF + HNO₃ in a screw-top Teflon beaker for 7 days at 100 °C (Liu et al., 1996). Trace elements of those samples were analyzed

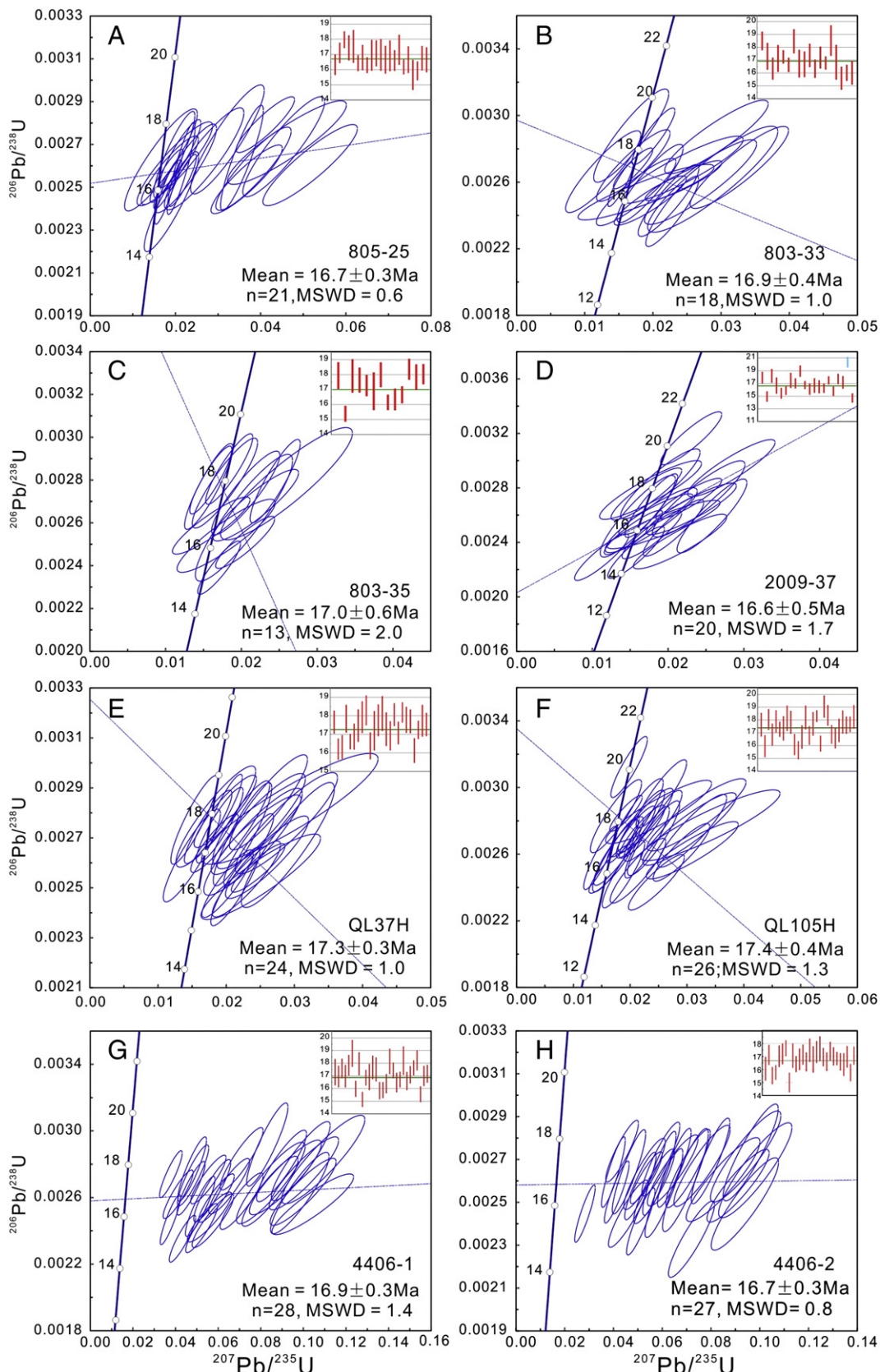


Fig. 4. Zircon concordia diagrams for the Qulong adakites.

by inductively coupled mass spectrometry (ICP-MS) at the State Key Laboratory of Isotope Geochemistry, Guangzhou Institute of Geochemistry, the Chinese Academy of Sciences, Guangzhou. The analytical uncertainty of the elements examined here was better than 5% for ICP-MS analysis, except for a few samples with low contents of trace elements for which the uncertainty was about 10%. The obtained values of trace elements in the AGV-3 standard are all consistent with their recommended values.

3.2. Zircon U-Pb dating

Zircon U-Pb dating and trace elements were analyzed using the LA-ICP-MS system in the State Key Laboratory of Isotope Geochemistry, Guangzhou Institute of Geochemistry, The Chinese Academy of Sciences. In this study, an Agilent 7500a ICP-MS coupled with a Resonetics RESolution M-50 laser-ablation system was used to analyze the U-Pb and trace elements of the zircons. The conditions were 80 mJ laser energy, a repetition rate of 8 Hz with a spot size of 31 μm in diameter and 50 s ablation time (Li et al., 2012a,b). A two-volume laser-ablation cell and a Squid smoothing device were used to improve the quality of data (Li et al., 2012a; Tu et al., 2011). Helium was used as carrier gas sampling ablation aerosols to the ICP source for Analysis. NIST SRM 610 and TEMORA were used as an external calibration standard, which were analyzed twice for every 10 analyses; and ^{29}Si as the internal standard to calculate the content of trace elements; TEMORA was analyzed 2 for every 5 analyses (Li et al., 2012a,b; Tu et al., 2011). ICPMSDataCal 8.3 was used to process the original test data was for isotope ratios and the content of trace elements (Liu et al., 2010b,c); Isoplot 3.23 (Ludwig, 2000) was used to calculate the U-Pb age and single spot data error is 1 σ , weighted average $^{206}\text{Pb}/^{238}\text{U}$ age is 2 σ . The obtained mean weighted $^{206}\text{Pb}/^{238}\text{U}$ age 416 ± 5.5 Ma (2 σ , MSWD = 0.5) from all the TEMORA zircons was obtained, which is consistent with the recommended values 416.75 ± 0.24 (Black et al., 2003), indicating that the data quality is reliable. Representative CL images and U-Pb concordia diagrams for zircon from the rock samples included in this study are shown in Figs. 3 and 4, respectively.

3.3. Zircon oxygen isotope

Zircon oxygen isotopes were analyzed in this study using a SHRIMP II ion microscope in the Beijing SHRIMP Center, Institute of Geology, Chinese Academy of Geological Sciences. About 200–300 grains for each sample were mounted to a one-inch diameter epoxy mount together with the zircon standard TEMORA (having a $\delta^{18}\text{O}$ value of 8.2‰) to correct instrumental mass fractionation (Black et al., 2004). Zircons were then polished down to near half section to get the internal structure exposed. The mount was vacuum-coated with a 500 nm layer of high-purity gold. The analytical procedure and operating conditions are similar to that of Ickert et al. (2008) and Trotter et al. (2008). During a typical analysis, a 3.0 nA beam of Cs^+ is focused into a spot of ~20 μm diameter on the target surface, generating an approximately 10⁹ cps $^{16}\text{O}^-$ secondary ion count. TEMORA was analyzed 3 times before every session during which a sequence of three samples was analyzed. Measured values of $\delta^{18}\text{O}$ are reported in the standard delta notation (per mil, ‰) relative to VSMOW. Under the above conditions, repeated runs of zircon standard TEMORA during the course of sample analysis yielded a mean $\delta^{18}\text{O}$ value of 8.19 ± 0.13 ‰ (2 σ ; n = 50), which is in good agreement with the previously reported value (8.2‰; Black et al., 2004).

3.4. Zircon Hf isotope

The in-situ Lu-Hf isotopic measurements of the zircon were performed by the LA-MC-ICPMS method using Thermo Finnigan Neptune multi-collector inductively coupled mass spectrometry (MC-ICP-MS) and a RESolution M50 laser ablation system at the State Key Laboratory

of Isotope Geochemistry, Guangzhou Institute of Geochemistry, Chinese Academy of Sciences. Lu-Hf isotopic analyses were obtained on the same zonation of zircon grains that were previously analyzed for O isotopes, with ablation pits of 40 μm in diameter, ablation time of 60 s, 15–20 J/cm² energy, and a repetition rate of 8 Hz. Detailed descriptions for the analytical techniques can be found in Wu and Yang (2006). The results of the $^{176}\text{Hf}/^{177}\text{Hf}$ analysis were normalized to $^{179}\text{Hf}/^{177}\text{Hf} = 0.7325$ using an exponential law for mass bias correction (Wu et al., 2006). During analysis, an isotopic ratio of $^{176}\text{Lu}/^{175}\text{Lu} = 0.02655$ and $^{176}\text{Yb}/^{172}\text{Yb} = 0.5887$ was applied (Chu et al., 2002; Wu et al., 2006). The measured $^{176}\text{Lu}/^{177}\text{Hf}$ ratios and the ^{176}Lu decay constant of $1.867 \times 10^{-1} \text{ yr}^{-1}$ reported by Soderlund et al. (2004) were used to calculate initial $^{176}\text{Lu}/^{177}\text{Hf}$ ratios. The chondritic values of $^{176}\text{Lu}/^{177}\text{Hf} = 0.0336$ and $^{176}\text{Hf}/^{177}\text{Hf} = 0.282785$ are adopted for the calculation of $\epsilon\text{Hf(t)}$ values, which were reported by Bouvier et al. (2008). The depleted mantle Hf model ages (T_{DM}) were calculated using the measured $^{176}\text{Lu}/^{177}\text{Hf}$ ratios of the zircon, based on the assumption that the depleted mantle reservoir has a linear isotopic growth from $^{176}\text{Hf}/^{177}\text{Hf} = 0.279718$ at 4.55 Ga to 0.283250 at present, with $^{176}\text{Lu}/^{177}\text{Hf} = 0.0384$ (Griffin et al., 2000).

3.5. Sr-Nd isotope

Whole rock Sr and Nd isotope ratios of the Qulong ore-bearing adakites were measured using a Multi-Collector Inductively-Coupled plasma Mass Spectrometry (MC-ICP-MS) at the State Key Laboratory of Isotope Geochemistry, Guangzhou Institute of Geochemistry, Chinese Academy of Sciences, after the procedures of (Liang et al., 2003; Wei et al., 2002). The $^{87}\text{Sr}/^{86}\text{Sr}$ and $^{143}\text{Nd}/^{144}\text{Nd}$ are calculated from the Rb, Sr, Sm and Nd contents measured by ICP-MS. Measured $^{87}\text{Sr}/^{86}\text{Sr}$ and $^{143}\text{Nd}/^{144}\text{Nd}$ values are normalized to $^{86}\text{Sr}/^{88}\text{Sr} = 0.1194$ and $^{146}\text{Nd}/^{144}\text{Nd} = 0.7129$ for mass fractionation. Long-term mean values of the Sr and Nd standards NBS standard 987 and JNd-1 of the laboratory are $^{87}\text{Sr}/^{86}\text{Sr} = 0.710249 \pm 5$ and $^{143}\text{Nd}/^{144}\text{Nd} = 0.512112 \pm 4$, respectively.

4. Results

4.1. Major and trace elements

Major and trace element compositions in representative samples of the Qulong adakites are given in Tables 1 and 2. The results are plotted in Figs. 5, 6 and 7, together with the data from previous studies. All the adakites studied have SiO_2 (60.20–70.77 wt.%), Al_2O_3 (12.10–16.46 wt.%), K_2O (2.46–6.18 wt.%), MgO (0.92–1.60 wt.%) and CaO (1.51–3.98 wt.%). Based on their chemical compositions, they mainly plot in the monzogranite and granodiorite areas (Fig. 5A). Compared to typical adakites from active continental arcs (Defant and Drummond, 1990; Kay, 1978; Ygodzinski et al., 1995), these samples have relatively high K_2O contents with most of the samples plotting in the high-K calc-

Table 1
Geochemical comparison of typical adakite and the Qulong adkite.

Typical adakite	Ore-bearing	Barren
High SiO_2 (≥ 56 wt.%)	60.2–79.3	63.0–70.1
High Al_2O_3 (≥ 15 wt.% at $\text{SiO}_2 = 70$ wt.%)	11.0–17.2	15.18–17.03
High Sr (>400 ppm)	259–1156	248–1195
Low Y (≤ 18 ppm)	1.91–9.12	5.04–8.8
Low Yb (≤ 1.9 ppm)	0.27–0.92	0.51–0.85
High Na_2O	0.23–6.0	3.95–6.6
High Sr/Y	50–202	49–178
High (La/Yb) _N	13.3–30.1	14.6–29.9

Adakite data: Defant and Drummond (1990).

Table 2

Representative major and trace element results of the Qulong adkite.

Sample	QL	QL	QL	QL	QL	QL	QL	001-	4406	4406	4406	2009	609	803	803	803	803	803	803	803	803	803	805	805	805			
	105H ^a	67H ^a	69H ^a	76H ^a	79H ^a	85H ^a	90H ^a	23A-1 ^b	-1 ^c	-2 ^c	-3 ^c	-4 ^c	-37 ^b	-38 ^c	-27 ^b	-28 ^b	-29 ^c	-30 ^c	-31 ^c	-32 ^c	-33 ^c	-34 ^b	-35 ^b	-36 ^c	-24 ^b	-25 ^b	-26 ^b	
Age	17.4 Ma								16.9 Ma	16.7 Ma			17.0 Ma	16.6 Ma	16.7 Ma								16.9 Ma	17.0 Ma	16.7 Ma			
Type	Barren adkite												Ore-bearing adkite															
SiO ₂	63.5	65.0	64.8	66.9	64.8	63.4	65.50	66.27	64.70	62.99	63.77	66.01	64.93	61.80	63.86	70.77	65.90	64.20	68.30	64.10	67.00	65.77	65.01	68.30	67.75	64.50	67.87	
TiO ₂	0.53	0.50	0.46	0.49	0.48	0.53	0.51	0.44	0.46	0.54	0.51	0.49	0.50	0.48	0.53	0.37	0.38	0.45	0.30	0.41	0.38	0.48	0.49	0.48	0.46	0.5	0.41	
Al ₂ O ₃	16.6	16.4	16.1	15.85	16.3	16.7	16.85	16.31	17.03	16.58	16.57	16.49	16.40	16.1	15.78	12.97	14.25	15.55	12.1	14.75	13.95	15.03	16.46	15.4	14.59	16.34	14.65	
Fe ₂ O ₃	3.57	3.33	3.05	3.28	3.47	3.48	2.11	4.32	4.85	3.97	3.62	4.09	2.1	2.08	1.5	1.75	1.92	0.98	1.69	1.77	1.66	1.59	2.04	1.67	2.26	1.44		
MnO	0.04	0.04	0.04	0.04	0.05	0.04	0.05	0.02	0.05	0.05	0.05	0.05	0.02	0.02	0.01	0.02	0.01	0.01	0.01	0.01	0.01	0.02	0.02	0.01	0.03	0.04	0.02	
MgO	1.55	1.52	1.35	1.43	1.50	1.62	1.56	1.35	1.47	1.72	1.61	1.31	1.42	1.41	1.51	1.16	1.18	1.21	0.92	1.18	1.01	1.50	1.60	1.32	1.50	1.29	1.17	
CaO	4.06	3.87	3.67	3.45	3.75	4.12	3.87	3.74	3.97	3.98	4.29	3.5	3.11	3.98	3.35	3.31	3.29	3.48	2.46	3.34	2.93	3.48	3.63	1.51	2.83	3.79	2.99	
Na ₂ O	6.55	4.81	6.33	4.49	6.15	6.40	4.91	4.20	4.72	4.55	4.7	4.44	3.99	5.95	3.47	3.54	4.86	4.29	2.77	5.35	3.27	3.77	4.22	4.15	3.17	3.95	3.55	
K ₂ O	2.54	2.75	2.77	3.02	2.73	2.58	2.69	3.50	1.42	2.70	2.67	3.17	2.9	3.28	4.55	3.74	4.2	4.03	6.18	4.07	5.07	4.45	3.9	4.91	5.68	4.04	4.97	
P ₂ O ₅	0.04	0.19	0.04	0.18	0.04	0.05	0.05	0.18	0.222	0.243	0.224	0.224	0.2	0.25	0.22	0.15	0.19	0.22	0.19	0.19	0.19	0.19	0.20	0.27	0.17	0.19	0.16	
SO ₃	/	/	/	/	/	/	/	/	<0.01	0.60	0.13	<0.01	/	1.99	/	/	1.87	1.89	1.53	1.69	1.64	/	/	1.17	/	/	/	
LOI	1.18	0.81	0.78	0.74	0.72	0.78	0.57	1.34	0.85	1.63	1.0	0.53	1.93	4.11	4.27	1.98	3.50	3.46	2.96	3.94	2.93	3.17	2.38	1.88	1.60	2.65	2.25	
Total	100.20	99.20	99.40	99.90	99.80	99.70	100.00	99.46	99.39	100.05	99.57	100.00	99.48	99.65	99.64	99.50	99.68	99.07	97.31	99.21	98.67	99.53	99.49	100.43	99.44	99.54	99.47	
Sc	/	/	/	/	/	/	/	5.24	5.6	6.3	5.8	5.5	5.02	5.1	5.1	3.2	4.2	4.3	3.0	4.2	3.6	4.9	5.1	4.3	4.4	4.8	3.6	
V	93	101	89	91	88	98	100	65.1	86	84	75	74	80.3	80.7	80.2	56.0	67.7	76.0	52.3	68.1	62.0	79.9	80.0	84.2	64.3	82.7	56.9	
Cr	10	10	10	10	10	10	10	16.7	13	26	12	14	10.8	11.2	10.5	11.2	11.7	10.8	7.6	9.7	18.3	10.0	12.2	10.4	10.1	9.8	8.9	
Co	8	8	7	7	8	9	9	6.10	12	16.8	8.8	7.4	10.1	5.97	7.25	7.00	6.42	8.33	6.10	4.16	5.33	4.82	6.35	4.10	8.48	5.14		
Ni	12	11	10	11	12	13	12	10.4	11.4	15.4	13.5	11.1	10.0	9.49	9.06	8.27	8.32	9.00	4.47	31.35	8.83	9.46	9.64	8.72	8.79	9.22	6.63	
Cu	3	9	7	44	25	6	93	5.86	18.6	3.6	4.2	3.7	712	4174	3524	3343	2992	2747	1323	2676	2825	3658	2322	6660	2793	2925	462	
Ga	21.5	21.6	21	20.5	21	22.2	21.4	18.4	23.6	24.1	22.5	22.4	19.9	19.5	19.0	14.8	17.5	20.0	14.0	17.5	14.1	16.7	19.5	18.5	16.7	18.4	16.8	
Rb	78.5	63.2	63.9	77.3	71.2	63.6	68.3	91.2	40.4	70.1	62.7	74.7	91.8	99.4	145.3	92.8	105.7	109.4	145.2	105.6	125.2	113.2	108.4	125.3	151	119.3	123.8	
Sr	1150	1140	1105	1035	1095	1175	1195	915	1065	1110	1055	1015	932	969.8	850.4	756.9	840.4	1156	590.4	856.8	694	893.6	936.2	837.4	722.1	874.2	824.9	
Y	8.8	7.6	6.2	7.6	6.5	7.8	7.5	8.14	7.2	7.5	7.1	6.3	7.41	6.44	6.01	4.96	5.97	5.73	4.47	6.36	5.46	6.46	6.52	5.50	5.69	6.75	5.14	
Zr	110	110	99	98	114	103	101	49.0	1.4	7.1	6.9	7.1	67.3	57.0	81.5	46.8	69.6	61.4	41.9	63.1	42.6	66.4	63.1	97.0	51.2	51.1	42.5	
Nb	4.4	4.1	3.4	3.9	3.5	4	3.5	3.89	3.8	4.3	4.1	4.3	3.8	3.51	3.63	2.94	3.04	3.52	3.03	2.85	3.55	3.90	3.99	3.73	3.24	4.23	3.08	
Cs	3.94	1.58	1.27	2.03	2.24	1.61	2.17	4.79	2.11	6.04	2.04	3.64	3.6	7.09	6.59	2.55	2.79	2.95	2.56	3.31	2.90	3.74	4.64	4.29	6.22	3.93	3.73	
Ba	674	750	768	756	737	759	896	831	450	710	640	720	705	583	707	629	644	903	747	681	648	584	616	863	646	732	727	
Hf	3.3	3.1	2.8	2.8	3.3	3	2.7	1.6	0.1	0.6	0.5	0.6	2.1	1.86	2.19	1.44	1.97	1.83	1.36	1.66	1.36	1.82	2.00	2.06	2.64	1.56	1.48	1.34
Ta	0.3	0.3	0.2	0.3	0.2	0.3	0.2	0.4	0.24	0.27	0.27	0.3	0.30	0.27	0.27	0.25	0.24	0.25	0.24	0.23	0.28	0.33	0.27	0.27	0.29	0.24		
Pb	13	14	15	13	15	14	14.3	11	14.2	13.6	13.3	17.1	31.6	26.5	29.3	39.7	29.5	31.6	38.9	36.6	47.9	29.5	33.9	43.5	123.0	26.9		
Th	7.49	7.41	5.78	8.31	7.19	7.86	5.09	8.7	3.7	6.8	5.9	6.7	8.24	5.29	4.92	5.03	5.44	8.14	6.28	3.62	7.09	5.95	5.62	8.14	6.57	5.27	6.74	
U	2.44	1.79	1.32	1.81	1.9	1.91	1.45	2.6	0.4	2.1	1.7	1.0	1.97	2.18	1.15	1.73	1.40	2.44	1.32	1.65	1.60	1.65	2.18	2.45	1.65	2.56	2.14	
La	25.4	23.4	20.1	23.6	20.8	23.3	21.1	26.8	13.1	19.1	19	19	21.3	21.26	17.81	15.75	15.9	32.43	16.4	15.39	16.08	21.3	20.05	19.98	22.72	21.98	16.75	
Ce	54.8	48.8	39.6	48	41.3	48	44.3	53.6	29.2	42.1	41	40	45.2	42.83	37.86	31.91	32.77	64.2	32.27	32.45	33.81	43.37	41.22	41.43	45.59	45.19	33.19	
Pr	6.68	5.64	4.58	5.66	4.83	5.67	5.22	6.5	3.65	5.38	5.07	5.73	5.37	4.964	4.1	4.078	7.725	4.065	4.259	4.37	5.367	5.35	5.437	5.72	5.707	4.108		
Nd	26.2	22.8	17.7	21.7	19	22.7	20.5	24.7	15.4	22.1	20.6	19.9	23.2	21.11	19.81	15.99	17.05	30.7	16.08	17.3	17.84	21.71	21.52	21.63	22.53	22.58	17.01	
Sm	4.53	3.79	3.24	3.83	3.46	4.08	3.83	3.8	2.91	3.98	3.62	3.41	3.77	3.468	3.236	2.691	2.872	4.435	2.567	2.942	2.914	3.462	3.46	3.557	3.526	3.704	2.733	
Eu	1.07	1.02	0.84	0.97	0.89	1.0	0.98	0.75	0.79	0.98	0.93	0.88	0.86	0.87	0.74	0.613	0.708	0.937	0.583	0.717	0.636</td							

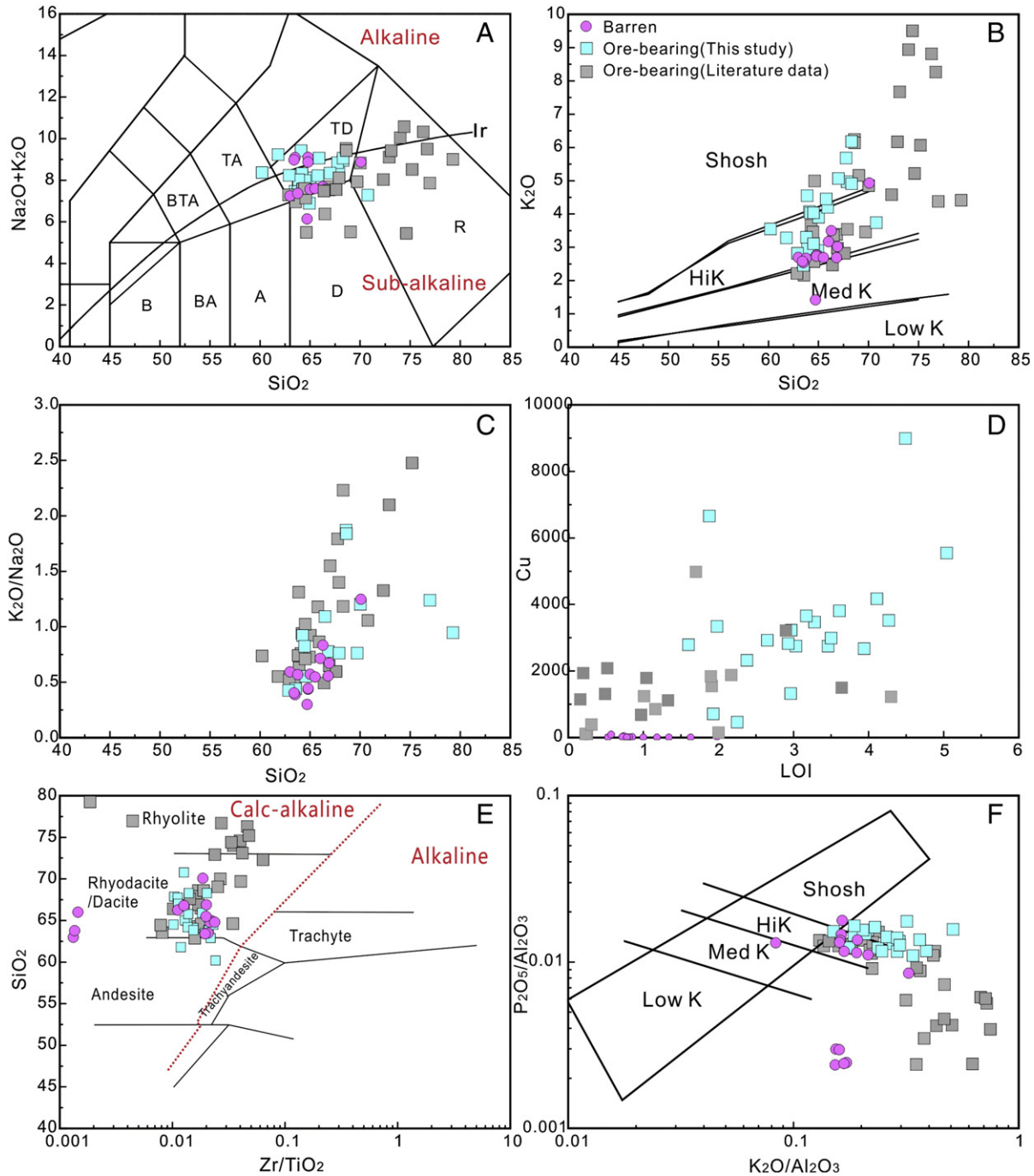


Fig. 5. TAS diagram of adakites from Qulong Miocene adakites following Le Maitre et al. (1989) (A). Solid curve from Irvine and Baragar (1971) separates alkaline from calc-alkaline lavas. B: Basalt; BA: basaltic andesite; A: andesite; D: dacite; BTA: basaltic trachyandesite; TA: trachyandesite; TD: trachydacite; R: rhyolite; plots of K_2O vs. SiO_2 (B); $\text{K}_2\text{O}/\text{Na}_2\text{O}$ vs. SiO_2 (C); Cu vs. LOI (D); Zr/Ti vs. SiO_2 (E) (Winchester and Floyd, 1977) and $\text{P}_2\text{O}_5/\text{Al}_2\text{O}_3$ vs. $\text{K}_2\text{O}/\text{Al}_2\text{O}_3$ (F) (Crawford et al., 2007) for the Qulong adakites. Data sources include Qu et al. (2010), Wang et al. (2006), Hou et al. (2005), Yang et al. (2008b) and this study.

alkaline and shoshonitic field in a K_2O versus SiO_2 diagram, marked variations in $\text{K}_2\text{O}/\text{Na}_2\text{O}$ ratios (Fig. 5C), showing high K calc-alkaline nature (Fig. 5B). Overall, the adakites display the same differentiation trends. The abundances of MgO , CaO , TiO_2 , Na_2O , TFe_2O_3 and Al_2O_3 decrease with increasing SiO_2 (Fig. 6A–F). With a few exceptions, K_2O correlates positively with SiO_2 (Fig. 5B). In both ore-bearing and barren adakites, the total alkaline contents ($\text{K}_2\text{O} + \text{Na}_2\text{O}$), K_2O abundance and $\text{K}_2\text{O}/\text{Na}_2\text{O}$ ratios show a positive correlation with SiO_2 (Fig. 5A, B and C), displaying the typical differentiation trend of calc-

alkaline arc magmas. However, some of the adakites have unusually high K_2O contents, yielding abnormally high total alkaline contents and $\text{K}_2\text{O}/\text{Na}_2\text{O}$ ratios. Consequently, these samples depart significantly from the overall trends (Fig. 5B and C), suggesting that the unusual K_2O enrichment was not simply a result of magmatic differentiation.

The samples have variable LOI contents, which show a positive relationship between Cu contents with few exceptions, with some being relatively high, especially the ore-bearing adakites (Fig. 5D).

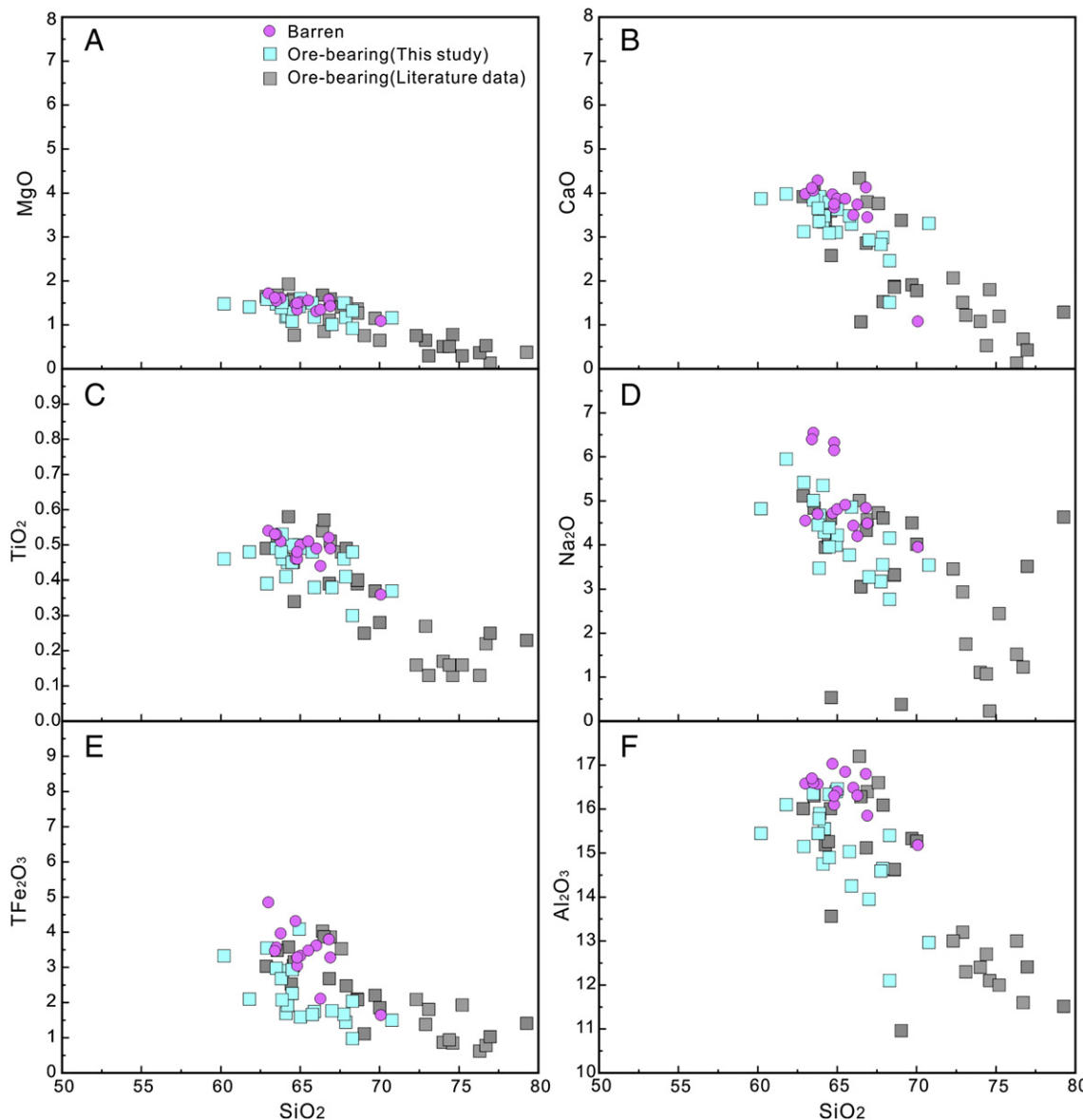


Fig. 6. Variation diagrams of major elements (wt.%) plotted against SiO_2 (wt.%) for the Qulong adakites.

This is consistent with our petrographic observations that these samples exhibit weak alteration. In order to better understand and classify the adakites based on their original compositions, it is necessary to assess and exclude the effects of subsequent hydrothermal alteration on the samples. To do so, the effects of element mobility are evaluated and then the more immobile elements, or derived parameters, are plotted versus SiO_2 on classification diagrams for the studied samples.

As shown in Figs. 5 and 6, the ore-bearing samples plot more scattered than the barren samples, with K_2O contents systematically higher than those of the barren samples (Fig. 5B, C and F). This is partially due to potassium addition during alteration. This metasomatism was most likely caused when hydrothermal K-feldspar and biotite formed during the early stage K-silicate alteration accompanying the widespread porphyry mineralization occurring throughout the Qulong district. In a total alkali versus SiO_2 diagram (TAS; Fig. 5A), samples from the ore-bearing adakites plot in both the trachydacite and rhyolite fields in composition. In contrast, the barren samples are

characterized by relatively low alkali contents and plot within the trachydacite field (Fig. 5A). Similarly, in the K_2O versus SiO_2 plot (Fig. 5B) samples from the ore-bearing adakites scatter throughout the high K to shoshonite fields, whereas the barren samples lie only within the Middle to high K field. Given the demonstrated mobility of K_2O illustrated above for the Qulong district, these schemes are unreliable for rocks having undergone hydrothermal alteration. Crawford et al. (2007) proposed that a plot of $\text{P}_2\text{O}_5/\text{Al}_2\text{O}_3$ versus $\text{K}_2\text{O}/\text{Al}_2\text{O}_3$ can be used to remove the effects of alteration. In a $\text{P}_2\text{O}_5/\text{Al}_2\text{O}_3$ versus $\text{K}_2\text{O}/\text{Al}_2\text{O}_3$ diagram (Fig. 5F), several samples do plot in low-K fields. Nevertheless, the majority of Qulong adakites, both ore-bearing and barren, plot in high-K field, whereas many ore-bearing adakites still plot in the shoshonite field, suggesting that high K is an original characteristic of Qulong adakites. In the Zr/TiO_2 versus SiO_2 diagram (Fig. 5E), most of the porphyry samples in this study were classified as calc-alkaline rather than alkaline, and plot in the andesite to rhyodacite fields. This is likely due to the addition of K_2O and SiO_2 during alteration.

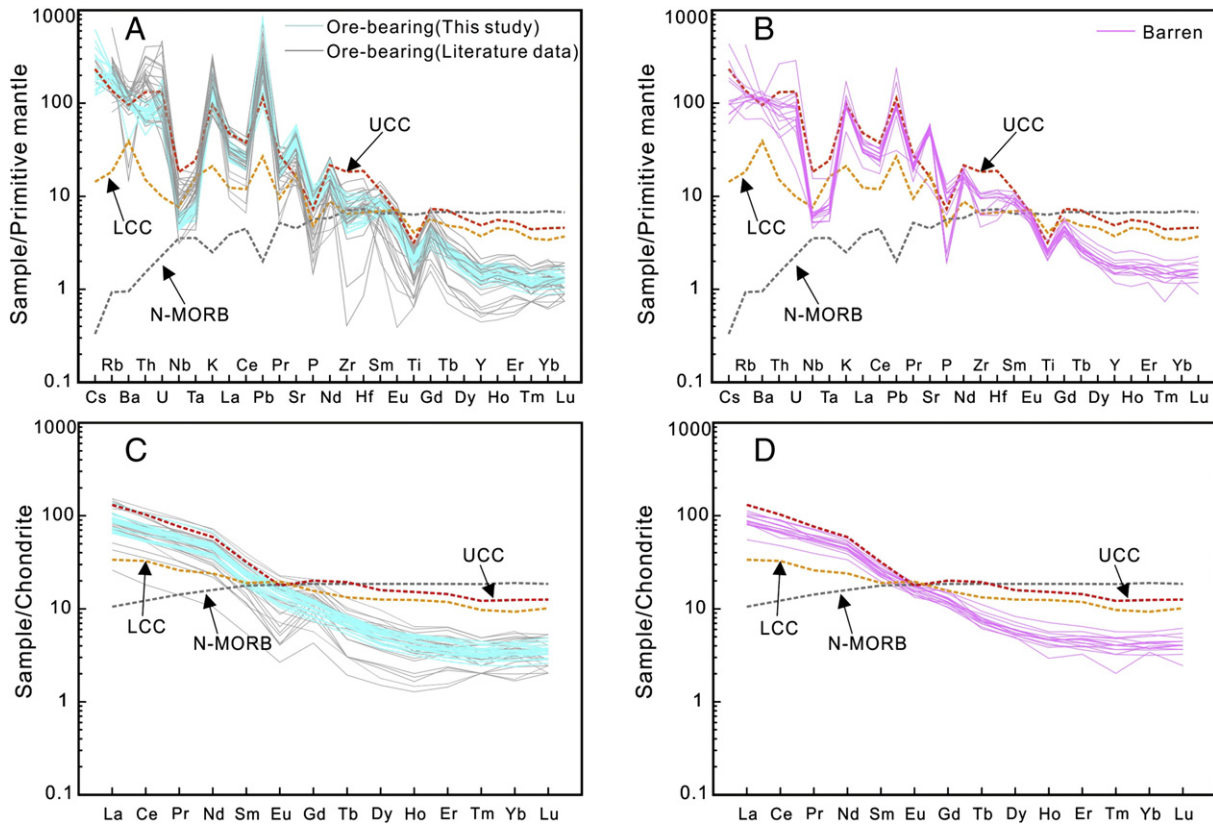


Fig. 7. Primitive mantle-normalized (Sun and McDonough, 1989) incompatible element diagrams (A, B) and chondrite-normalized rare earth element diagrams (C, D) for the Qulong adakites. Also shown are lower continental crust (LCC), upper continental crust (UCC) and normal MORB (N-MORB) using dotted lines.

The most notable characteristics of the Qulong adakites are that the ore-bearing and barren adakites share similar incompatible element and rare earth element patterns, enrichment in incompatible elements such as large ion lithophile elements (LILE) (Fig. 7A, B), light rare earth elements (LREE) (Fig. 7A, B), and depleted in high field strength elements (HFSE) and heavy rare earth elements (HREE) (Fig. 7). Primitive mantle normalized incompatible trace element patterns (Fig. 7A,

B) reveal marked negative Nb, Ta, P and Ti anomalies and positive Pb anomalies, and a majority of samples show weak or no-Eu anomalies, reflecting a typical characteristic of subduction-related magmas. However, the ore-bearing adakites have systematically higher Rb (76.1–391.0 ppm) and Pb (17.1–123 ppm) and slightly lower average Zr (69.5 ppm) contents than the barren adakites (Rb: 40.4–118.3 ppm, Pb: 4.7–35.6 ppm, and Zr: 89.3 ppm). All the adakites have high Sr

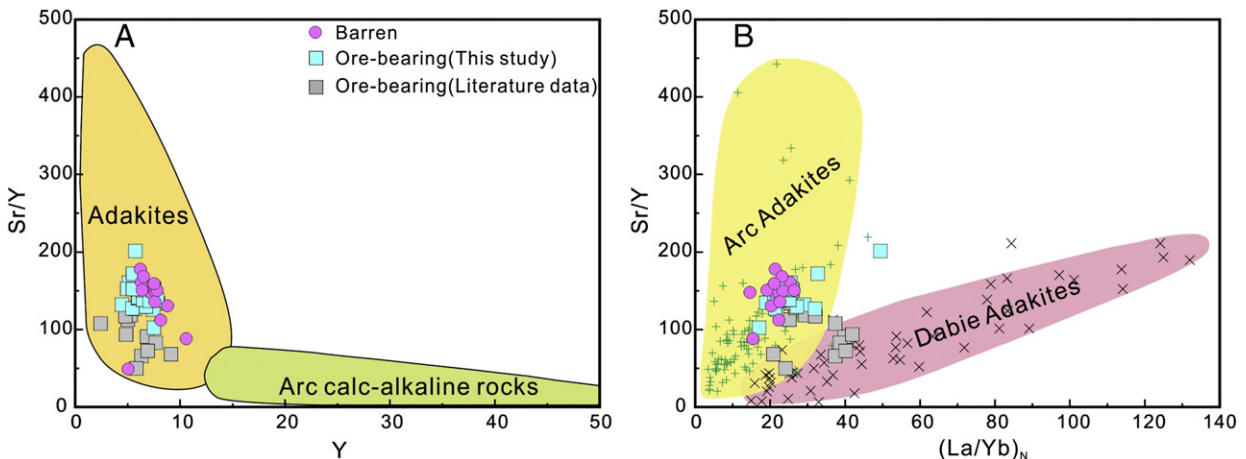


Fig. 8. (A) Sr/Y versus Y for the Qulong adakites. Fields of adakites and normal calc-alkaline magmas are from Defant and Drummond (1990). (B) Sr/Y versus $(La/Yb)_n$ for the Qulong adakites modified from Liu et al. (2010a) and Ling et al. (2013a), illustrating the differences between arc adakites from circum-Pacific region and Tibet and Dabie adakites.

contents, and display distinct positive Sr anomalies (Fig. 7A, B) with low HREE and Y content. Thus, the adakites display high Sr/Y and $(La/Yb)_n$ ratios, which show geochemical affinities similar to those of modern adakites (Fig. 8) (Defant and Drummond, 1990; Ling et al., 2013a; Liu et al., 2010a; Sun et al., 2012a). These adakites are enriched in LREEs and most of these lack significant negative Eu anomalies, reflecting both the presence of residual garnet and the absence of plagioclase in the source region (Fig. 7C, D) (Defant and Drummond, 1990; Kay, 1978; Sun et al., 2012a).

4.2. Zircon U-Pb geochronology

The zircon U-Pb isotopic data are given in [Appendix Table](#). The zircons from Qulong ore-bearing adakites have crystal lengths of ~100–450 μm with length-to-width ratios of 2:1 to 5:1. Almost all the zircons have narrow and frequent oscillatory zoning (Fig. 3). Zircons from these samples yield $^{206}\text{Pb}/^{238}\text{U}$ weighted mean ages of 16.7 ± 0.3 Ma, 16.9 ± 0.4 Ma, 17.0 ± 0.6 Ma and 16.6 ± 0.5 Ma, respectively (Fig. 4A–D; 2σ error). The zircons from Qulong barren adakites have morphological characteristics similar to those from the ore-bearing ones. Similarly, zircons from barren adakites yield $^{206}\text{Pb}/^{238}\text{U}$ weighted mean ages of 17.3 ± 0.3 Ma, 17.4 ± 0.4 Ma, 16.9 ± 0.3 Ma and 16.7 ± 0.3 Ma, respectively (Fig. 4E–H; 2σ error). Thus, in-situ zircon U-Pb dating of these samples suggests that the ore-bearing adakites were generated contemporaneous with the barren adakites.

4.3. Zircon oxygen isotopes

The zircon oxygen isotopic compositions of the Qulong ore-bearing and barren adakites are relatively homogeneous, with $\delta^{18}\text{O} = 5.1\text{--}7.3\text{\textperthousand}$ ($n = 68$, average $6.4\text{\textperthousand}$) and $4.0\text{--}7.4\text{\textperthousand}$ ($n = 33$; average $6.3\text{\textperthousand}$), respectively ([Table 3](#)). The cumulative probability-histogram of $\delta^{18}\text{O}$ yields a unimodal distribution with a peak at about $6.5\text{\textperthousand}$ (Fig. 9). In summary, zircon oxygen isotopic compositions are relatively homogenous.

4.4. Zircon Hf isotope

Zircons from the Qulong ore-bearing and barren adakites have $^{176}\text{Hf}/^{177}\text{Hf}$ varying from 0.282828 to 0.283068 and 0.282932 to 0.283038 respectively ([Table 3](#)).

The zircon $\epsilon\text{Hf}(t)$ values of the ore-bearing and barren adakites, which were corrected to the crystallization age based on their individual spot $^{206}\text{Pb}/^{238}\text{U}$ ages, range from 1.9 to 10.4 ($n = 66$, average 7.7%) and from 5.6 to 9.3 ($n = 31$, average 7.5%), respectively, with corresponding two-stage Hf model ages of 767–329 Ma and 577–384 Ma, respectively. The cumulative probability-histogram of $\epsilon\text{Hf}(t)$ yields a unimodal distribution with a mode at about 7.6 (Fig. 10A). Fig. 11 shows the variation of $\delta^{18}\text{O}$ versus $\epsilon\text{Hf}(t)$ values of zircons from the Qulong adakites. Most of these zircons have similar $\epsilon\text{Hf}(t)$ and $\delta^{18}\text{O}$ values, with high $\delta^{18}\text{O}$ values higher than the mantle value and $\text{Hf}(t)$ values close to depleted mantle field.

4.5. Sr-Nd isotope

Whole rock Sr-Nd isotope composition data for the Qulong adakites are listed in [Table 4](#). The Qulong ore-bearing adakites have a wide range of initial $^{87}\text{Sr}/^{86}\text{Sr}$ ratios, varying from 0.704904 to 0.705053 and the Nd isotopic compositions with $\epsilon\text{Nd}(t)$ varying from –0.04 to 0.61 ([Table 4](#)). The Sr and Nd isotope of Qulong ore-bearing adakites are plotted in Fig. 12. Also plotted are literature data for Jurassic porphyries from Qulong (Yang et al., 2011), Cretaceous adakites from Mamen (Zhu et al., 2009), LiziZong volcanics (Mo et al., 2008) and Miocene adakites (Gao et al., 2010b; Hou et al., 2004b, 2013; Qin et al., 2014; Xu et al., 2010) and fields of Indus-Yalung ophiolites (Miller et al., 2003; Niu et al., 2006; Xu and Castillo, 2004; Zhang et al., 2005), ancient Lhasa

basement rocks (Zhu et al., 2012a) and ultrapotassic rocks from south Tibet (Gao et al., 2007a; Liu et al., 2014; Miller et al., 1999; Zhao et al., 2009). The Nd-isotope model ages (T_{DM}) of the Qulong adakites range from 0.62 to 0.71 Ga ([Table 4](#)). In view of our preferred petrogenetic model, we draw attention to the observation that within the Sr-Nd array, the Qulong adakites occupy an area close to Yarlung Tsangpo MORB (Fig. 12).

5. Discussion

5.1. Formation of Gangdese adakites

The nature of magma sources for the Miocene adakitic magmatism in the Gangdese terrane has been a topic of debate (Chung et al., 2003; Gao et al., 2003b, 2007b; Guo et al., 2007; Hou et al., 2003, 2004a,b; Qu et al., 2004; Xu et al., 2010). Four models have been proposed for the origins of the Qulong and other Gangdese adakites and their high Sr/Y so far. These include: (1) partial melting of the subducted Neotethyan oceanic crust, followed by interaction with the overlying mantle wedge (Gao et al., 2003a; Hou et al., 2003, 2004c; Qu et al., 2004); (2) partial melting of the thickened and then delaminated Lhasa mafic lower crust (Chung et al., 2003) or a newly formed mafic lower crust (Hou et al., 2004a,b; Li et al., 2011); (3) partial melting of an upper mantle source metasomatized by slab-derived melts (Gao et al., 2007b); and (4) partial melting of the subducted Indian continental crust beneath the southern Lhasa terrane (Xu et al., 2010). These genetic models can be tested using the petrologic and geochemical characteristics, such as high Sr/Y, La/Yb ratios and the zircon Hf-O and Sr-Nd isotopic signatures.

According to the model of partial melting of thickened Lhasa lower crust or juvenile mafic intermediate lower crust of the Lhasa terrane (Chung et al., 2003; Guo et al., 2007; Hou et al., 2004a), a thickened Lhasa crust (>50 km) must exist prior to the high Sr/Y magmatism. This model plausibly explains the formation of barren adakites older than 20 Ma (Chung et al., 2003, 2005), but is not necessarily true for Qulong and other porphyry deposits. For example, the exposed Lhasa crustal basement and the Lhasa lower crust both have much higher radiogenic Sr and non-radiogenic Nd isotopic compositions than the Qulong adakites ($(^{87}\text{Sr}/^{86}\text{Sr})_i < 0.706$ and $\epsilon\text{Nd} > -0.3$; Fig. 12) (Hou et al., 2004b and this study). The former, is represented by silicic metavolcanic rocks from central Lhasa subterrane (492 Ma), with $(^{87}\text{Sr}/^{86}\text{Sr})_t (t = 16 \text{ Ma}) > 0.751$ and $\epsilon\text{Nd} < -12$ (Zhu et al., 2012a), and the latter, assumed by Miller et al. (1999), with $(^{87}\text{Sr}/^{86}\text{Sr})_i = 0.7100$ and $\epsilon\text{Nd} = -22$ ($^{143}\text{Nd}/^{144}\text{Nd} = 0.5115$). If these exposed Lhasa crustal basement or the Lhasa lower crust is representative, depleted components are needed for the Qulong adakites. Furthermore, although the Tibetan plateau has been thickened to approximately twice the thickness of normal continental crust based on geophysical data (ca. 70–80 km; Molnar, 1990; Molnar et al., 1998; Owens and Zandt, 1997), whether it had achieved such a thickness by the Miocene is still under debate. For example, Nomade et al. (2004) suggested that there was a much thinner crust of ca. 35 km in south Tibet during Miocene. Thus, the thickened modern south Tibetan crust is not a robust indicator of the partial melting of metabasalt in the lower crust during the Miocene. In fact, the crustal thickness in the Andes reaches 68 km (Chiaradia, 2014), however, adakites associated with porphyry Cu deposits are all slab melts (Sun et al., 2010), which are closely related to the subduction of oceanic ridges (Cooke et al., 2005; Sun et al., 2010).

Partial melting of juvenile mafic lower crust was criticized by previous authors. Gao et al. (2010b) suggested that none of the exposed Lhasa crustal basement or the juvenile crust could adequately explain the magma derivation for the Gangdese adakites. Obviously, in spite of their wider ranges in Sr-Nd isotope compositions, many of the Qulong adakites have higher Sr-Nd isotopic compositions than that of the Linzizong volcanic rocks (Fig. 12), which may be equivalent to the

Table 3

In-situ zircon Hf–O isotopic composition for the Qulong adakites.

Spot no.		Age(Ma)	$^{176}\text{Lu}/^{177}\text{Hf}$	$^{176}\text{Hf}/^{177}\text{Hf}$	$\text{eHf}_{(\text{T})}$	T_{DM} (Ma)	$T_{\text{DM}}\text{C}$ (Ma)	$\delta^{18}\text{O}(\text{\textperthousand})$	$\pm 2\delta$	$\delta^{18}\text{O}_{\text{wr}}$
805-25										
805-25-01	r	16.3	0.000541	0.283017	8.57	328	422	5.95	0.15	7.4
805-25-04	r	17.4	0.000431	0.283042	9.45	293	377	6.65	0.11	8.1
805-25-06	r	17.5	0.000501	0.283034	9.2	304	391	6.87	0.11	8.32
805-25-08	r	16.4	0.000572	0.283021	8.72	323	414	6.57	0.13	8.02
805-25-10	r	19.6	0.000898	0.283022	8.82	324	412	6.64	0.1	8.09
805-25-12	r	17	0.000549	0.283054	9.87	277	355	6.52	0.09	7.97
805-25-13	r	17.1	0.000481	0.283057	10.01	271	348	6.68	0.12	8.13
805-25-14	r	17	0.000357	0.28304	9.38	295	381	6.96	0.15	8.41
805-25-15	r	16.7	0.000351	0.283024	8.81	318	410	5.93	0.18	7.38
805-25-16	r	16.9	0.000587	0.283037	9.3	300	385	6.93	0.11	8.38
805-25-18	r	17.3	0.000337	0.283068	10.39	255	329	6.12	0.13	7.57
805-25-20	r	16.7	0.000469	0.283028	8.94	313	403	6.3	0.15	7.75
805-25-21	r	15.7	0.000455	0.283033	9.11	305	394	6.44	0.07	7.89
805-25-23	r	15.9	0.000449	0.283036	9.24	301	387	7.3	0.09	8.75
805-25-24	r	16.8	0.00051	0.282995	7.8	359	462	6.38	0.14	7.83
803-33										
803-33-04	r	18.5	0.00062	0.283003	8.12	349	447	6.39	0.09	7.99
803-33-05	r	17.3	0.000507	0.283039	9.36	297	382	6.88	0.08	8.48
803-33-07	r	16.8	0.000452	0.282997	7.86	356	460	6.22	0.1	7.82
803-33-08	r	17.1	0.000332	0.283016	8.54	329	424	6.99	0.1	8.59
803-33-09	r	17.3	0.000466	0.283044	9.53	290	373	6.65	0.13	8.25
803-33-12	r	18.5	0.000411	0.283036	9.27	301	388	7.05	0.15	8.65
803-33-14	r	16.7	0.000713	0.282981	7.3	381	488	6.29	0.07	7.89
803-33-16	r	16	0.000369	0.282999	7.91	353	456	6.6	0.14	8.2
803-33-17	r	16.7	0.000364	0.28301	8.34	336	434	7.04	0.09	8.64
803-33-19	r	16.4	0.000386	0.283028	8.94	312	403	6.48	0.13	8.08
803-33-20	r	17.2	0.000451	0.283006	8.21	343	442	6.54	0.08	8.14
803-33-21	r	18.4	0.000496	0.283002	8.08	349	449	5.63	0.11	7.23
803-33-22	r	16.8	0.000764	0.282979	7.22	384	492	6.93	0.15	8.53
803-33-24	r	16.9	0.000446	0.28296	6.55	408	527	6.31	0.07	7.91
803-33-25	r	15.6	0.000528	0.28301	8.31	338	435	6.87	0.13	8.47
803-33-26	r	16	0.000714	0.283001	7.98	353	453	6.45	0.12	8.05
803-33-27	r	16						6.29	0.1	7.89
803-35										
803-35-01	r	17.9	0.000571	0.283009	8.3	341	437	6.62	0.15	8.1
803-35-03	r	15.4	0.000649	0.282978	7.17	384	494	6.46	0.1	7.94
803-35-04	r	17.9	0.000486	0.282977	7.18	384	495	6.85	0.16	8.33
803-35-06	r	17.6	0.000568	0.282941	5.91	435	561	6.97	0.15	8.45
803-35-09	r	17.3	0.000512	0.282989	7.61	367	473	6.16	0.05	7.64
803-35-11	r	16.9	0.000647	0.282947	6.11	428	550	5.08	0.12	6.56
803-35-13	r	18	0.00058	0.282959	6.53	411	528	6.26	0.1	7.74
803-35-15	r	17.2	0.000649	0.282957	6.47	414	532	5.76	0.08	7.24
803-35-16	r	16.2	0.000485	0.282983	7.36	376	485	6.65	0.12	8.13
803-35-17	r	16.4	0.000504	0.282975	7.09	387	499	5.97	0.2	7.45
803-35-18	r	16.7	0.00047	0.282964	6.7	402	519	6.44	0.23	7.92
803-35-20	r	19.8	0.000629	0.282963	6.73	405	520	5.64	0.16	7.12
803-35-21	r	17.4	0.00051	0.282942	5.94	433	559	6.17	0.12	7.65
803-35-22	r	17	0.000299	0.283001	8.01	349	451	6.83	0.09	8.31
803-35-23	r	18.4	0.000487	0.282944	6.03	431	555	6.51	0.11	7.99
803-35-25	r	17.8	0.000598	0.282943	5.99	433	557	6.05	0.14	7.53
803-35-26	r	18	0.000451	0.282947	6.12	426	550	5.46	0.08	6.94
2009-37										
2009-37-01	r	17.8	0.000421	0.283008	8.26	341	439	5.92	0.08	7.39
2009-37-03	r	16.2	0.000569	0.282957	6.45	414	532	6.93	0.2	8.4
2009-37-04	r	15	0.000485	0.282978	7.15	383	495	5.51	0.17	6.98
2009-37-05	r	18.2	0.000526	0.282965	6.77	401	517	5.81	0.14	7.28
2009-37-06	r	16.7	0.000553	0.283013	8.43	334	430	5.9	0.12	7.37
2009-37-07	r	15.5	0.000434	0.282983	7.33	376	485	6.29	0.1	7.76
2009-37-08	r	15.9	0.000529	0.282981	7.28	379	488	6.67	0.13	8.14
2009-37-10	r	17.5	0.000549	0.282997	7.89	356	458	6.07	0.16	7.54
2009-37-11	r	19.3						5.88	0.09	7.35
2009-37-12	r	16.3	0.000503	0.282949	6.18	424	547	6.66	0.09	8.13
2009-37-13	r	17	0.000572	0.283017	8.57	329	423	6.22	0.11	7.69
2009-37-16	r	19	0.000956	0.282828	1.92	601	767	6.25	0.09	7.72
2009-37-17	r	16.8	0.000692	0.282986	7.47	374	479	6.31	0.13	7.78
2009-37-18	r	16.1	0.000594	0.282918	5.05	468	604	6.22	0.13	7.69
2009-37-19	r	16.7	0.000385	0.283016	8.53	329	425	6.12	0.11	7.59
2009-37-21	r	16.5	0.00068	0.282966	6.78	402	516	5.54	0.15	7.01
2009-37-24	r	15.8	0.000476	0.282942	5.9	433	560	5.83	0.15	7.3
2009-37-25	r	17.7	0.000486	0.283008	8.28	341	438	6.19	0.11	7.66
2009-37-26	r	17.7	0.000466	0.28292	5.17	464	599	6.04	0.14	7.51

Table 3 (continued)

Spot no.		Age(Ma)	$^{176}\text{Lu}/^{177}\text{Hf}$	$^{176}\text{Hf}/^{177}\text{Hf}$	$\text{eHf}_{(\text{T})}$	T_{DM} (Ma)	T_{DMC} (Ma)	$\delta^{18}\text{O}(\text{\textperthousand})$	$\pm 2\delta$	$\delta^{18}\text{Owr}$
<i>QL37H</i>										
QL37H-01	r	17.5	0.000416	0.283038	9.33	298	384	6.47	0.29	7.94
QL37H-03	r	17.3	0.000434	0.282996	7.85	357	460	6.50	0.36	7.97
QL37H-07	r	17.9	0.000509	0.282958	6.51	411	530	6.13	0.56	7.59
QL37H-08	r	16.4	0.000381	0.282973	7.00	389	503	6.19	1.06	7.66
QL37H-09	r	18.7	0.000528	0.282953	6.36	418	538	5.91	0.91	7.38
QL37H-11	r	17.0	0.000522	0.282978	7.19	383	494	6.12	0.18	7.59
QL37H-14	r	16.3	0.000695	0.282993	7.70	364	467	6.32	0.43	7.79
QL37H-15	r	17.2	0.000622	0.283017	8.59	329	422	6.47	0.40	7.94
QL37H-17	r	17.9	0.000412	0.283010	8.34	338	435	5.29	0.57	6.76
QL37H-20	r	17.3	0.000467	0.282981	8.70	378	468	6.37	0.35	7.84
QL37H-21	r	17.4	0.000496	0.282994	7.78	360	464	6.79	0.58	8.26
QL37H-23	r	16.4	0.000529	0.283005	8.14	345	444	5.90	0.53	7.36
QL37H-24	r	18.2	0.000635	0.282987	7.56	371	476	7.02	0.50	8.49
QL37H-25	r	16.2	0.000546	0.282968	6.82	398	513	7.21	0.25	8.68
QL37H-27	r	18.8	0.000615	0.282980	7.29	382	490	6.37	0.52	7.84
<i>QL105H</i>										
QL105H-01	r	17.6	0.000778	0.282993	7.75	364	466	7.37	0.30	8.75
QL105H-03	r	18.1	0.000461	0.282992	7.71	363	468	6.52	0.20	7.91
QL105H-05	r	17.9	0.000551	0.282932	5.61	447	577	5.25	0.37	6.64
QL105H-06	r	18.9	0.000632	0.282985	7.49	374	480	6.10	0.44	7.49
QL105H-07	r	17.3	0.000827	0.282974	7.05	392	501	5.85	0.67	7.24
QL105H-08	r	17.4	0.000458	0.282981	7.31	379	488	6.45	0.28	7.84
QL105H-11	r	18.1	0.000486	0.282961	6.63	406	524	5.47	0.66	6.86
QL105H-12	r	17.8	0.000467	0.282979	7.24	382	492	6.91	0.25	8.30
QL105H-13	r	18.1	0.000583	0.282995	7.81	361	463	6.48	0.33	7.86
QL105H-14	r	16.1	0.000613	0.282949	6.15	425	547	6.65	0.40	8.03
QL105H-16	r	16.7	0.000498	0.282995	7.80	359	462	6.23	0.19	7.61
QL105H-17	r	16.3	0.000696	0.282982	7.32	380	487	6.72	0.39	8.11
QL105H-18	r	18.2	0.000540	0.282993	7.74	363	467	7.09	0.35	8.47
QL105H-20	r	17.7	0.000565	0.282989	7.60	368	473	6.09	0.36	7.47
QL105H-23	r	16.2	0.000494	0.282969	6.85	396	511	4.00	2.14	5.38
QL105H-25	r							6.43	0.35	7.81
QL105H-26	r	19.1	0.000462	0.283009	8.32	340	437	6.56	0.14	7.94
QL105H-27	r	18.4						6.24	0.39	7.63

Notes: r-zircon rim.

juvenile crust in the Lhasa terrane during the Eocene (Mo et al., 2007). Moreover, the Miocene adakites occur in an E–W trending 1500 km-long narrow belt along the Yarlung Tsangpo suture zone, whereas the voluminous Linzizong volcanic rocks mainly crop out north of the adakite belt. It was argued that if the Miocene adakites were derived from the remelting of thickened lower crust, they should also be distributed everywhere throughout the Lhasa block like Linzizong volcanic

rocks, rather than only along a narrow belt (Gao et al., 2010b). All these need to be addressed.

A third model suggested that the Gangdese Miocene adakites were derived from an upper mantle source metasomatized by slab-derived melts (Gao et al., 2007b). However, metasomatized mantle peridotite consists mainly of pyroxenite. Partial melting of pyroxenite forms basalts, rather than adakites.

In a Sr/Y versus (La/Yb)n diagram (Fig. 8B), most of the samples plot in the low end of circum-Pacific field, close to Dabie adakites. Several ore-bearing samples plot in the field of Dabie adakites. These characteristics support the involvement of crustal materials, i.e., partial melting of both subducted slab and the lower continental crust. Given that partial melting of the lower continental crust forms magmas with low initial Cu contents (Sun et al., 2011, 2012a), these support that ore-bearing adakites are not necessarily the ore-forming ones.

The Qulong ore-bearing adakites have highly variable Nb/Ta values (7.4–24.5), whereas Nb/Ta of barren adakites is much less varied (11.0–17.9). Niobium and Ta were taken as geochemical twins that do not fractionate from each other during mantle magmatism (with Nb/Ta value of 17.7; Sun and McDonough, 1989). Nevertheless, Nb and Ta do fractionate from each other during crustal processes (Ding et al., 2009, 2013; Foley et al., 2002; Liang et al., 2009; Xiao et al., 2006). Mid-ocean ridge basalts have fairly constant Nb/Ta of ~17 (with Nb/Ta value of 17.7; Sun and McDonough, 1989) whereas the continental crust has Nb/Ta of ~12–13 in average and ~8 in the lower crust (with Nb/Ta value of 8.0; Rudnick and Gao, 2003). Partial melting of MORB eclogite forms melt with Nb/Ta up to ~25 (Foley et al., 2002). Therefore, slab melts with variable crustal contamination plausibly explain the Nb/Ta ratios of Qulong adakites.

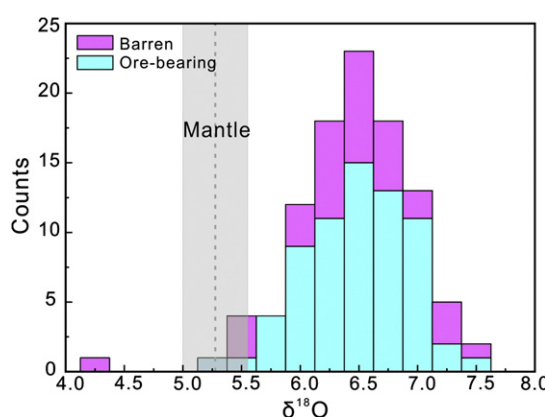


Fig. 9. The cumulative probability histogram of in-situ zircon oxygen isotopic compositions ($\delta^{18}\text{O}_{\text{zn}}$) of Qulong ore-bearing and barren adakites. The gray bar represents the normal-mantle $\delta^{18}\text{O}_{\text{zn}}$ range. Data are reported in Table 3.

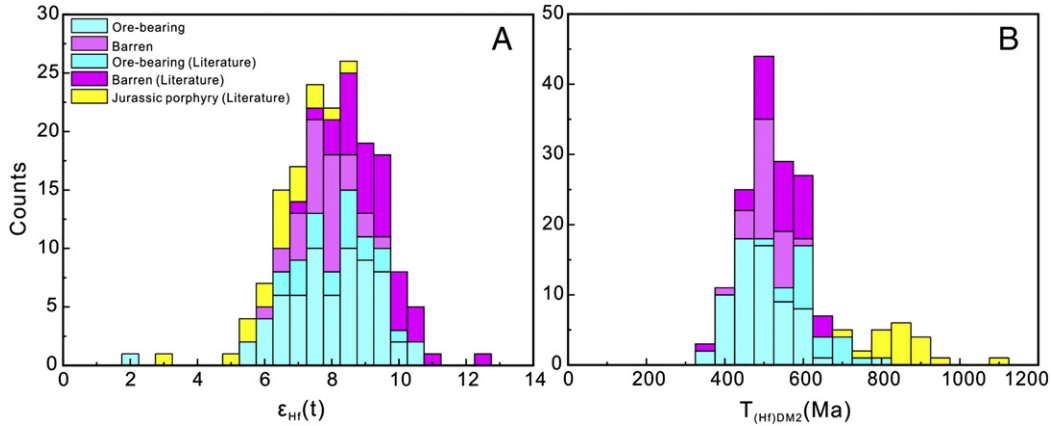


Fig. 10. The cumulative probability histogram of in-situ zircon $\epsilon_{\text{Hf}}(t)$ (A) and T_{DM2} (B) for the Qulong ore-bearing and -barren adakites. Data sources are from Yang et al. (2011), Chung et al. (2009), Yang (2008) and this study. Data of this study are reported in Table 3. There is no systematic difference between our data and literature data. We also added Hf of zircon from Jurassic granite in the region, which is systematically more enriched.

This is compatible with our new in-situ zircon O and Hf isotope data. The Hf–O isotope correlations (Fig. 11) may be plausibly explained as the mixing of components with mantle-like isotopes (e.g., subducted oceanic crust) with continental crust (e.g., S-type granites). According to simulation results, continental crust material contributed about 10%–30% of the zircon O and Hf isotope values (Fig. 11), implying addition of continental crust materials into the slab-derived adakite melt. In detail, the majority of zircon $\delta^{18}\text{O}$ values for the Qulong adakites are homogeneous with a narrow range of 5.1% to 7.4% and an average of 6.4%, close to the mantle $\delta^{18}\text{O}$ value of zircon (Valley et al., 2005). The whole-rock values calculated based on the formula of $\delta^{18}\text{O}_{\text{Zrn}}-\text{WR} = \delta^{18}\text{O}_{\text{Zrn}}-\delta^{18}\text{O}_{\text{WR}} \approx -0.0612$ (wt.% SiO₂) + 2.5 (Valley et al., 2005)

range from 6.6 to 8.8. Also, Yang and Hou (2009) once reported similar $\delta^{18}\text{O}$ values ranging from 7.2 to 8.3% for quartz fluid inclusions associated with early stage alteration of Qulong adakites indicating a magmatic origin.

5.2. Qulong adakites and the porphyry Cu deposit

As mentioned above, Qulong adakites are different from circum-Pacific adakites in several aspects. First, Qulong adakites have MgO lower than 2 wt.%, which is much lower than ore-forming adakites from the circum-Pacific region. Qulong adakites also have much higher K₂O and SiO₂, which again is rare for adakites that form porphyry Cu deposits. Moreover, the ore-bearing and barren adakites have similar geochemical characteristics. The barren adakites have very low Cu contents of less than 100 ppm. All these suggest that neither the ore-bearing nor the barren adakites so far sampled from Qulong porphyry deposit are responsible to the Cu deposit. In other words, the ore-forming porphyry is not sampled in this study. This is supported by the systematic older zircon U–Pb ages (16.4 ± 0.4 – 17.7 ± 0.3 Ma) of Qulong adakitic samples so far studied than the Re–Os isochron ages (15.36 ± 0.21 – 16.41 ± 0.48 Ma) (Fig. 13; Hou et al., 2009; Li and Rui, 2004; Meng et al., 2003b; Rui et al., 2003). However, Qin et al. (2014) analyzed zircons from ore-bearing adakitic monzogranite porphyry and obtained the age of 15.3 ± 0.6 Ma, which is identical to the Re–Os isochron ages within error, and these adakites may be the most likely ‘ore-forming adakites’. Rocks earlier than these ore-bearing adakitic monzogranite porphyries may be only ‘ore-bearing’ adakites.

6. Conclusions

The Qulong adakites studied here are characterized by higher K₂O and SiO₂ and lower MgO, compared to circum-Pacific adakites. Consistently, the Qulong adakites plot mainly in the lower end of the field defined by circum-Pacific adakites in the Sr/Y versus (La/Yb)_n diagram with a few samples that plot away from the fields defined by circum-Pacific adakites (slab melts) and even into Dabie adakites fields, which imply significant involvement of continental crust components. Ore-bearing and barren adakite samples studied here have geochemical characteristics very similar to each other. These results argue that these ore-bearing and barren adakites have similar origins.

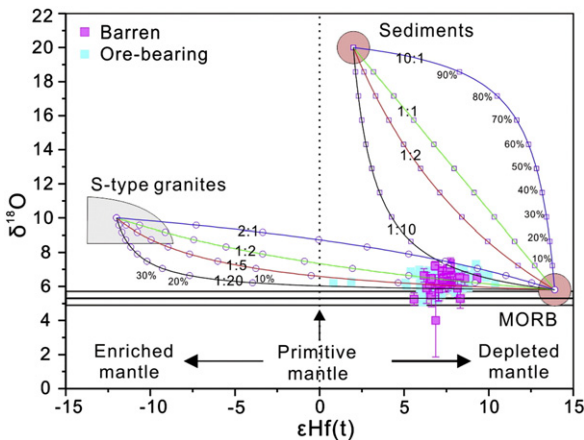


Fig. 11. In-situ zircon $\delta^{18}\text{O}$ vs $\epsilon_{\text{Hf}}(t)$ isotopes plot of the Qulong adakites. Hafnium isotope sources include: Chauvel et al. (2008) for MORB and sediments; oxygen isotopes of MORB and marine sediments are from Hoefs (2009). The compositions of the members for mixing calculations are: (1) MORB: $\delta^{18}\text{O} = 5.8\text{‰}$, $\epsilon_{\text{Hf}} = 13.9$; (2) marine sediments: $\delta^{18}\text{O} = 20\text{‰}$, $\epsilon_{\text{Hf}} = 2$; (3) S-type granites: $\delta^{18}\text{O} = 10\text{‰}$, $\epsilon_{\text{Hf}} = -12$; the mixing curves were constructed using different $\text{Hf}_{\text{MORB}}/\text{Hf}_{\text{sediments}}$ and $\text{Hf}_{\text{MORB}}/\text{Hf}_{\text{S-type granites}}$ elemental ratios from 1:10 to 10:1 and 1:2 to 20:1 respectively. Error bars depict the average 2σ uncertainty. The smooth curves denote the two component mixing trends between MORB and marine sediments and S-type granites. $\text{Hf}_{\text{MORB}}/\text{Hf}_{\text{sediments}}$ and $\text{Hf}_{\text{MORB}}/\text{Hf}_{\text{S-type granites}}$ are the ratios of the Hf concentration (ppm) in MORB to that in the marine sediments and S-type granites respectively, which are indicated for each curve. The open circles and squares on mixing curves are at 10% intervals. All data are listed in Table 3.

Table 4

Sr and Nd isotope data for the Qulong adakites.

Sample	T(Ma)	Rb	Sr	$^{87}\text{Rb}/^{86}\text{Sr}$	$^{87}\text{Sr}/^{86}\text{Sr}$	2δ	$^{87}\text{Sr}/^{86}\text{Sr(i)}$	Sm	Nd	$^{147}\text{Sm}/^{144}\text{Nd}$	$^{143}\text{Nd}/^{144}\text{Nd}$	2δ	$^{143}\text{Nd}/^{144}\text{Nd(i)}$	$\epsilon\text{Nd(t)}$	$T_{\text{DM}}(\text{Ga})$
805-25	16.7	119	874	0.4002	0.705050	6	0.704958	3.70	22.58	0.0997	0.512626	5	0.512615	-0.04	0.71
805-26		124	825	0.4401	0.705065	7	0.704956	2.73	17.01	0.0977	0.512641	5	0.512630	0.28	0.67
803-30		109	1156	0.2775	0.705120	4	0.705053	4.44	30.70	0.0878	0.512642	5	0.512632	0.32	0.62
803-31		145	590	0.7212	0.705193	5	0.705019	2.57	16.08	0.0970	0.512628	5	0.512618	0.03	0.69
803-33	16.9	125	694	0.5290	0.705092	5	0.704965	2.91	17.84	0.0993	0.512639	4	0.512628	0.23	0.68
803-35	17.0	108	936	0.3396	0.705036	5	0.704954	3.46	21.52	0.0977	0.512640	5	0.512629	0.25	0.67
803-36		125	837	0.4388	0.705124	6	0.705016	3.56	21.63	0.1000	0.512644	5	0.512633	0.33	0.68
2009-37	16.6	91.8	932	0.2888	0.704975	4	0.704904	3.77	23.22	0.0988	0.512640	5	0.512629	0.25	0.68
609-38	16.7	99.4	970	0.3005	0.705016	6	0.704944	3.47	21.11	0.0999	0.512659	12	0.512648	0.61	0.66

Parameters and corrected formula as follows: $(^{87}\text{Sr}/^{86}\text{Sr})_i = (^{87}\text{Sr}/^{86}\text{Sr})_s + ^{87}\text{Rb}/^{86}\text{Sr}(e^{\lambda t} - 1)$, $\lambda = 1.42 \times 10^{-11} \text{ a}^{-1}$; $(^{143}\text{Nd}/^{144}\text{Nd})_i = (^{143}\text{Nd}/^{144}\text{Nd})_s + (^{147}\text{Sm}/^{144}\text{Nd}) \times (e^{\lambda t} - 1)$, $\epsilon\text{Nd(t)} = [(^{143}\text{Nd}/^{144}\text{Nd})_s / (^{143}\text{Nd}/^{144}\text{Nd})_{\text{CHUR}}(t) - 1] \times 10^4$, $T_{\text{DM}} = 1/\lambda \times \ln \{[(^{143}\text{Nd}/^{144}\text{Nd})_s - (^{143}\text{Nd}/^{144}\text{Nd})]\}$.

Oxygen isotopes of zircons from the ore-bearing and barren adakites are similar, with $\delta^{18}\text{O}$ ranging from 4.0 to 7.4‰, which are close to the mantle value (5.3‰). Consistently, $\epsilon\text{Hf(t)}$ ranges from 1.9 to 10.4‰. These in-situ zircon Hf-O isotopic measurements for the most samples yield a binary mixing trend between mantle- and crustal-derived melts, with mantle-related sources as the main contributor.

Qulong is taken as the largest porphyry copper deposit closely related to adakites formed in post-collisional period in Tibet, formed between 15.36 ± 0.21 – 16.41 ± 0.48 Ma (Re-Os isochron ages). Both the ore-bearing and barren adakites are systematically older (16.6 ± 0.5 – 17.4 ± 0.4 Ma), and thus are not responsible to the porphyry mineralization. The adakitic porphyry with the age of 15.3 ± 0.6 Ma in the central phase is responsible to the Cu mineralization.

Acknowledgments

We would like to thank Guangwu Jiang for his assistance in the field. We thank Ning Li and Yu Liu for help during SHRIMP zircon oxygen isotope analysis and Le Zhang for zircon Hf isotope. We also thank Ying Liu, Guoqian Hu and Jinlong Ma for help during whole rock major element, trace element and Sr-Nd isotope analysis. This study is supported by the National Natural Science Foundation of China (Nos. 41090374, 41121002, 41172080, 41103012). This is contribution No. IS-0000 from GIGCAS.

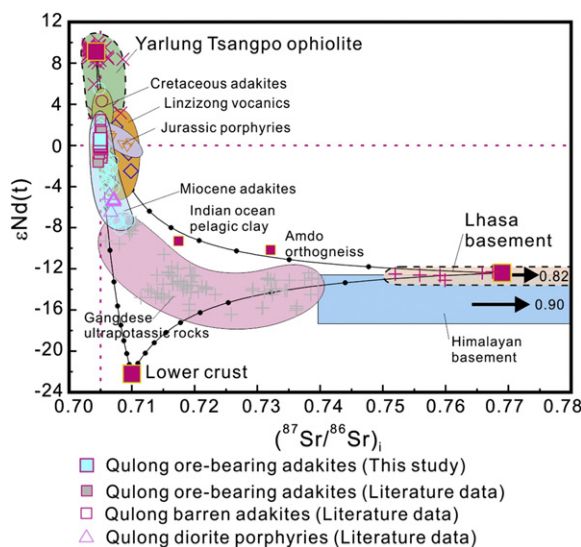


Fig. 12. $\epsilon\text{Nd(t)}$ vs. $(^{87}\text{Sr}/^{86}\text{Sr})_i$ diagrams for Qulong adakites. Data sources are as follows: Qulong adakites (Hou et al., 2004b; Qin et al., 2014) and this study, Gangdese Miocene adakites (Gao et al., 2010a; Hou et al., 2004b, 2012; Wang et al., 2010; Xu et al., 2010), Yarlung Tsangpo ophiolite (Miller et al., 2003; Niu et al., 2006; Xu and Castillo, 2004; Zhang et al., 2005), Linzizong volcanic rocks (Gao et al., 2008; Mo et al., 2007), Indian Ocean pelagic sediment (Benothman et al., 1989), Himalayan basement (Vidal et al., 1982). Cretaceous adakites: Zhu et al. (2009); Jurassic porphyries: Yang et al. (2011); Miocene adakites: Gao et al. (2010b), Hou et al. (2013), Hou et al. (2004b) and Wang et al. (2010). Lhasa crustal basement and the lower crust component of the Lhasa terrane proposed by Zhu et al. (2012a) and Miller et al. (1999) respectively. Indian Ocean pelagic sediment is used as a proxy for Neo-Tethyan sediment.

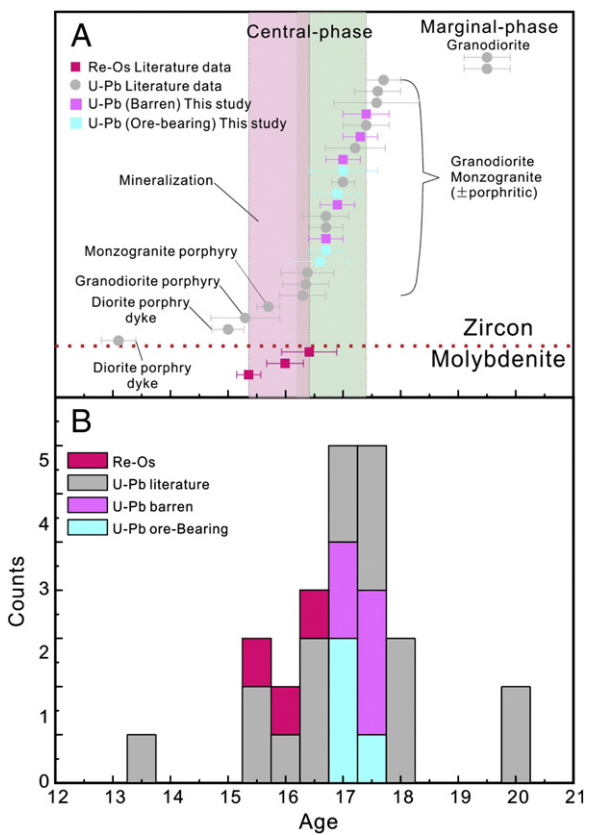


Fig. 13. Radiometric age data (A) and these cumulative probability histograms (B) of Miocene adakites and mineralization at Qulong. Zircon U-Pb age of the Qulong adakites is from Li and Rui (2004); Mo et al. (2006); Qin et al. (2014); Wang et al. (2006); Yang (2008) and this study. Molybdenite Re-Os age is from Li and Rui (2004); Meng et al. (2003b); and Zheng et al. (2004).

Appendix A

Appendix Table

LA-ICPMS zircon U-Pb isotope data of Qulong adakites.

Appendix Table (continued)

Sample	Pb	Th	U	Th/U	$^{207}\text{Pb}/^{235}\text{U}$	$^{207}\text{Pb}/^{235}\text{U}$	$^{206}\text{Pb}/^{238}\text{U}$	$^{206}\text{Pb}/^{238}\text{U}$	$^{206}\text{Pb}/^{238}\text{U}$	$^{206}\text{Pb}/^{238}\text{U}$
	ppm	ppm	ppm		Ratio	1sigma	Ratio	1sigma	Age (Ma)	1sigma
200937-19	0.6	89	169	0.53	0.02580	0.00304	0.00259	0.00018	16.7	1.2
200937-21	0.9	130	250	0.52	0.01778	0.00401	0.00256	0.00016	16.5	1.0
200937-22	1.4	183	427	0.43	0.01942	0.00493	0.00253	0.00012	16.3	0.8
200937-23	2.3	464	601	0.77	0.02272	0.00288	0.00272	0.00010	17.5	0.6
200937-24	1.3	254	418	0.61	0.01786	0.00260	0.00246	0.00012	15.8	0.7
200937-26	1.3	233	363	0.64	0.01714	0.00308	0.00276	0.00013	17.7	0.8
200937-32	1.0	167	285	0.59	0.01779	0.00230	0.00267	0.00015	17.2	1.0
200937-35	2.1	415	492	0.84	0.02305	0.00267	0.00316	0.00013	20.4	0.8
200937-38	1.3	233	414	0.56	0.01123	0.00236	0.00229	0.00011	14.8	0.7
<i>QL37H</i>										
QL37H-01	1.0	107	300	0.36	0.01735	0.00230	0.00274	0.00010	17.7	0.6
QL37H-02	1.0	100	321	0.31	0.02021	0.00249	0.00252	0.00009	16.2	0.6
QL37H-03	1.0	137	296	0.46	0.02297	0.00331	0.00254	0.00010	16.3	0.6
QL37H-04	0.9	92	254	0.36	0.01534	0.00228	0.00277	0.00012	17.8	0.8
QL37H-06	5.6	2436	1228	1.98	0.02468	0.00260	0.00258	0.00006	16.6	0.4
QL37H-08	1.2	167	341	0.49	0.02599	0.00402	0.00262	0.00011	16.9	0.7
QL37H-10	1.1	134	323	0.41	0.02240	0.00283	0.00271	0.00014	17.5	0.9
QL37H-11	1.2	151	338	0.45	0.01848	0.00386	0.00279	0.00013	17.9	0.9
QL37H-13	1.0	95	264	0.36	0.02620	0.00378	0.00284	0.00013	18.3	0.8
QL37H-14	1.0	171	303	0.56	0.02508	0.00579	0.00254	0.00011	16.4	0.7
QL37H-15	0.8	120	227	0.53	0.02904	0.00451	0.00267	0.00017	17.2	1.1
QL37H-17	0.6	79	152	0.52	0.02882	0.00495	0.00276	0.00013	17.8	0.9
QL37H-19	0.9	143	242	0.59	0.02934	0.00855	0.00282	0.00015	18.1	0.9
QL37H-21	0.7	133	206	0.64	0.02393	0.00477	0.00268	0.00014	17.3	0.9
QL37H-23	0.8	136	244	0.56	0.01496	0.00277	0.00263	0.00012	16.9	0.8
QL37H-24	1.2	159	327	0.49	0.01986	0.00302	0.00281	0.00010	18.1	0.6
QL37H-25	1.4	334	387	0.86	0.02330	0.00241	0.00265	0.00009	17.1	0.6
QL37H-26	2.1	177	599	0.30	0.01980	0.00169	0.00283	0.00009	18.2	0.5
QL37H-30	1.0	142	266	0.53	0.02220	0.00276	0.00276	0.00011	17.8	0.7
QL37H-31	0.9	156	243	0.64	0.01906	0.00226	0.00275	0.00010	17.7	0.6
QL37H-32	0.8	120	247	0.49	0.02135	0.00238	0.00251	0.00010	16.1	0.7
QL37H-33	1.7	345	477	0.72	0.01829	0.00231	0.00268	0.00008	17.2	0.5
QL37H-36	0.9	145	260	0.56	0.02470	0.00456	0.00276	0.00013	17.7	0.9
QL37H-37	1.1	184	313	0.59	0.02481	0.00406	0.00272	0.00010	17.5	0.6
<i>QL105H</i>										
QL105H-01	1.2	187	305	0.61	0.03093	0.00400	0.00274	0.00014	17.6	0.9
QL105H-02	0.7	118	242	0.49	0.01883	0.00247	0.00248	0.00013	16.0	0.9
QL105H-03	0.7	94	188	0.50	0.02270	0.00320	0.00280	0.00013	18.1	0.8
QL105H-04	1.1	130	321	0.41	0.01795	0.00289	0.00262	0.00014	16.9	0.9
QL105H-05	1.5	237	425	0.56	0.02180	0.00282	0.00278	0.00013	17.9	0.9
QL105H-07	2.7	514	752	0.68	0.01875	0.00187	0.00269	0.00009	17.3	0.6
QL105H-08	0.6	86	170	0.51	0.02413	0.00304	0.00270	0.00015	17.4	1.0
QL105H-10	1.5	121	372	0.33	0.01981	0.00212	0.00312	0.00012	20.1	0.8
QL105H-11	1.2	146	336	0.43	0.02113	0.00310	0.00282	0.00015	18.1	1.0
QL105H-12	0.8	104	206	0.51	0.02402	0.00338	0.00277	0.00014	17.8	0.9
QL105H-14	0.7	87	216	0.40	0.02138	0.00324	0.00250	0.00013	16.1	0.8
QL105H-15	1.2	232	335	0.69	0.02462	0.00325	0.00243	0.00011	15.7	0.7
QL105H-16	0.8	117	225	0.52	0.01742	0.00266	0.00259	0.00014	16.7	0.9
QL105H-18	1.1	167	284	0.59	0.01750	0.00297	0.00283	0.00014	18.2	0.9
QL105H-19	1.2	198	316	0.63	0.02902	0.00329	0.00261	0.00011	16.8	0.7
QL105H-20	0.9	134	219	0.61	0.03046	0.00544	0.00275	0.00014	17.7	0.9
QL105H-22	3.4	411	927	0.44	0.01926	0.00189	0.00284	0.00007	18.3	0.5
QL105H-23	1.1	168	370	0.45	0.01648	0.00247	0.00251	0.00010	16.2	0.6
QL105H-26	1.4	209	371	0.57	0.02549	0.00294	0.00296	0.00014	19.1	0.9
QL105H-27	1.0	175	253	0.69	0.02501	0.00617	0.00285	0.00013	18.4	0.8
QL105H-29	0.9	120	262	0.46	0.03093	0.00535	0.00262	0.00011	16.9	0.7
QL105H-30	1.4	236	420	0.56	0.01478	0.00195	0.00258	0.00013	16.6	0.8
QL105H-31	0.6	98	171	0.57	0.02297	0.00259	0.00267	0.00014	17.2	0.9
QL105H-32	0.8	117	176	0.67	0.03410	0.00811	0.00277	0.00014	17.9	0.9
QL105H-33	0.9	147	253	0.58	0.02209	0.00265	0.00274	0.00010	17.6	0.7
QL105H-34	1.3	198	373	0.53	0.02104	0.00224	0.00275	0.00009	17.7	0.6
QL105H-36	0.8	122	210	0.58	0.03168	0.00575	0.00284	0.00014	18.3	0.9
<i>ZK4406-1</i>										
ZK4406-1.01	0.5	77	166	0.46	0.08473	0.01064	0.00269	0.00016	17.3	1.0
ZK4406-1.02	0.6	87	171	0.51	0.09988	0.01023	0.00263	0.00013	17.0	0.9
ZK4406-1.03	1.2	161	379	0.42	0.04824	0.00483	0.00273	0.00012	17.6	0.8
ZK4406-1.05	0.7	114	225	0.51	0.08435	0.00870	0.00264	0.00014	17.0	0.9
ZK4406-1.06	1.0	139	307	0.45	0.04782	0.00443	0.00277	0.00013	17.8	0.8
ZK4406-1.07	0.7	121	184	0.66	0.08307	0.00638	0.00292	0.00016	18.8	1.1
ZK4406-1.08	1.4	255	415	0.61	0.05597	0.00688	0.00248	0.00010	16.0	0.6
ZK4406-1.09	0.8	160	208	0.77	0.08975	0.00773	0.00279	0.00014	18.0	0.9
ZK4406-1.11	1.2	241	431	0.56	0.04327	0.00409	0.00235	0.00009	15.1	0.6

(continued on next page)

Appendix Table (continued)

Sample	Pb ppm	Th ppm	U ppm	Th/U	$^{207}\text{Pb}/^{235}\text{U}$ Ratio	$^{207}\text{Pb}/^{235}\text{U}$ 1sigma	$^{206}\text{Pb}/^{238}\text{U}$ Ratio	$^{206}\text{Pb}/^{238}\text{U}$ 1sigma	$^{206}\text{Pb}/^{238}\text{U}$ Age (Ma)	$^{206}\text{Pb}/^{238}\text{U}$ 1sigma
ZK4406-1										
ZK4406-1.12	1.5	258	466	0.55	0.04123	0.00464	0.00262	0.00010	16.9	0.6
ZK4406-1.13	0.5	76	169	0.45	0.09834	0.00906	0.00263	0.00016	16.9	1.0
ZK4406-1.14	0.6	98	178	0.55	0.10024	0.01076	0.00275	0.00014	17.7	0.9
ZK4406-1.15	0.7	114	238	0.48	0.09156	0.01117	0.00272	0.00015	17.5	1.0
ZK4406-1.16	1.2	230	408	0.56	0.05757	0.00645	0.00246	0.00011	15.8	0.7
ZK4406-1.17	1.3	224	442	0.51	0.03759	0.00313	0.00247	0.00010	15.9	0.6
ZK4406-1.18	1.0	164	351	0.47	0.05158	0.00460	0.00255	0.00012	16.4	0.8
ZK4406-1.19	0.5	82	173	0.47	0.09878	0.00913	0.00282	0.00016	18.1	1.0
ZK4406-1.20	1.4	226	453	0.50	0.05541	0.00549	0.00271	0.00010	17.4	0.6
ZK4406-1.21	0.7	96	221	0.44	0.10445	0.01267	0.00256	0.00012	16.5	0.8
ZK4406-1.22	1.3	237	414	0.57	0.05924	0.00551	0.00260	0.00010	16.7	0.6
ZK4406-1.23	0.6	81	180	0.45	0.10930	0.01290	0.00283	0.00018	18.2	1.1
ZK4406-1.24	0.8	157	257	0.61	0.07104	0.00666	0.00258	0.00011	16.6	0.7
ZK4406-1.25	1.4	238	427	0.56	0.04731	0.00435	0.00266	0.00011	17.1	0.7
ZK4406-1.26	1.9	359	585	0.61	0.03782	0.00350	0.00274	0.00009	17.6	0.6
ZK4406-1.27	0.7	112	229	0.49	0.07103	0.00665	0.00283	0.00012	18.2	0.8
ZK4406-1.28	1.1	230	384	0.60	0.05227	0.00495	0.00242	0.00010	15.6	0.6
ZK4406-1.29	1.2	223	370	0.60	0.05723	0.00573	0.00264	0.00012	17.0	0.8
ZK4406-1.30	0.9	120	289	0.41	0.06517	0.00633	0.00267	0.00011	17.2	0.7
ZK4406-2										
ZK4406-2.01	0.5	94	177	0.53	0.09389	0.00912	0.00249	0.00014	16.0	0.9
ZK4406-2.02	0.8	149	232	0.64	0.07060	0.00602	0.00266	0.00012	17.1	0.8
ZK4406-2.03	0.6	89	174	0.51	0.10898	0.01408	0.00275	0.00015	17.7	1.0
ZK4406-2.04	0.8	144	277	0.52	0.05120	0.00385	0.00241	0.00010	15.5	0.7
ZK4406-2.05	1.8	486	577	0.84	0.02829	0.00277	0.00245	0.00009	15.8	0.6
ZK4406-2.06	1.0	221	309	0.71	0.04635	0.00452	0.00264	0.00013	17.0	0.8
ZK4406-2.07	0.7	98	220	0.45	0.07632	0.00762	0.00267	0.00013	17.2	0.8
ZK4406-2.08	1.2	153	380	0.40	0.04354	0.00443	0.00274	0.00010	17.6	0.6
ZK4406-2.09	0.8	120	253	0.47	0.07198	0.00624	0.00233	0.00012	15.0	0.8
ZK4406-2.10	0.5	84	166	0.51	0.09816	0.00993	0.00265	0.00015	17.1	0.9
ZK4406-2.11	1.3	264	418	0.63	0.04133	0.00335	0.00255	0.00010	16.4	0.6
ZK4406-2.12	0.6	97	189	0.51	0.08496	0.00998	0.00261	0.00013	16.8	0.8
ZK4406-2.13	0.5	76	164	0.47	0.10703	0.01274	0.00256	0.00014	16.5	0.9
ZK4406-2.14	0.7	101	237	0.43	0.06496	0.00454	0.00266	0.00012	17.1	0.8
ZK4406-2.15	1.0	211	298	0.71	0.05666	0.00552	0.00257	0.00011	16.6	0.7
ZK4406-2.16	0.6	77	184	0.42	0.09422	0.00954	0.00271	0.00014	17.5	0.9
ZK4406-2.17	0.6	84	204	0.41	0.06952	0.00619	0.00260	0.00016	16.8	1.0
ZK4406-2.18	0.6	125	189	0.66	0.07980	0.00520	0.00269	0.00013	17.3	0.8
ZK4406-2.19	0.5	90	165	0.54	0.09627	0.00747	0.00273	0.00015	17.6	1.0
ZK4406-2.20	1.0	134	332	0.40	0.05272	0.00560	0.00263	0.00011	16.9	0.7
ZK4406-2.21	0.5	73	172	0.42	0.09111	0.00842	0.00258	0.00011	16.6	0.7
ZK4406-2.22	0.9	113	296	0.38	0.05943	0.00515	0.00270	0.00011	17.4	0.7
ZK4406-2.23	1.1	163	351	0.46	0.03996	0.00321	0.00264	0.00011	17.0	0.7
ZK4406-2.24	1.3	201	404	0.50	0.05346	0.00432	0.00262	0.00008	16.8	0.5
ZK4406-2.25	0.9	146	301	0.49	0.05106	0.00426	0.00258	0.00010	16.6	0.7
ZK4406-2.26	0.9	164	284	0.58	0.06068	0.00512	0.00254	0.00014	16.4	0.9
ZK4406-2.27	0.7	101	194	0.52	0.11166	0.01746	0.00274	0.00013	17.6	0.8
ZK4406-2.28	0.7	83	233	0.36	0.05884	0.00452	0.00264	0.00013	17.0	0.8
ZK4406-2.29	1.3	192	424	0.45	0.04609	0.00539	0.00245	0.00010	15.8	0.7
ZK4406-2.30	0.9	129	273	0.47	0.06431	0.00688	0.00265	0.00011	17.1	0.7

References

- Allegre, C.J., Courtillot, V., Tappognier, P., Hirn, A., Mattauer, M., Coulon, C., Jaeger, J.J., Achache, J., Scharer, U., Marcoux, J., Burg, J.P., Girardeau, J., Armijo, R., Gariepy, C., Gopel, C., Li, T.D., Xiao, X.C., Chang, C.F., Li, G.Q., Lin, B.Y., Teng, J.W., Wang, N.W., Chen, G.M., Han, T.L., Wang, X.B., Den, W.M., Sheng, H.B., Cao, Y.G., Zhou, J., Qiu, H.R., Bao, P.S., Wang, S.C., Wang, B.X., Zhou, Y.X., Ronghua, X., 1984. Structure and evolution of the Himalaya-Tibet orogenic belt. *Nature* 307, 17–22.
- Audley-Charles, M.G., Ballantyne, P.D., Hall, R., 1988. Mesozoic-Cenozoic rift-drift sequence of Asian fragments from Gondwanaland. *Tectonophysics* 155, 317–330.
- Benothman, D., White, W.M., Patchett, J., 1989. The geochemistry of marine-sediments, island-arc magma genesis, and crust mantle recycling. *Earth and Planetary Science Letters* 94, 1–21.
- Black, L.P., Kamo, S.L., Allen, C.M., Aleinikoff, J.N., Davis, D.W., Korsch, R.J., Foudoulis, C., 2003. TEMORA 1: a new zircon standard for Phanerozoic U-Pb geochronology. *Chemical Geology* 200, 155–170.
- Black, L.P., Kamo, S.L., Allen, C.M., Davis, D.W., Aleinikoff, J.N., Valley, J.W., Mundil, R., Campbell, I.H., Korsch, R.J., Williams, I.S., Foudoulis, C., 2004. Improved $^{206}\text{Pb}/^{238}\text{U}$ microprobe geochronology by the monitoring of a trace-element-related matrix effect; SHRIMP, ID-TIMS, ELA-ICP-MS and oxygen isotope documentation for a series of zircon standards. *Chemical Geology* 205, 115–140.
- Bouvier, A., Vervoort, J.D., Patchett, P.J., 2008. The Lu-Hf and Sm-Nd isotopic composition of CHUR: constraints from unequilibrated chondrites and implications for the bulk composition of terrestrial planets. *Earth and Planetary Science Letters* 273, 48–57.
- Chang, C.F., Zhang, S.L., 1973. Tectonic fatures of the Mount Jolmo Lungma region in southern Tibet, China. *Scientia Geologica Sinica* 1, 1–12 (in Chinese with English abstract).
- Chauvel, C., Lewin, E., Carpentier, M., Arndt, N.T., Marini, J.-C., 2008. Role of recycled oceanic basalt and sediment in generating the Hf-Nd mantle array. *Nature Geoscience* 1, 64–67.
- Chiariadis, M., 2014. Copper enrichment in arc magmas controlled by overriding plate thickness. *Nature Geoscience* 7, 43–46.
- Chu, N.C., Taylor, R.N., Chavagnac, V., Nesbitt, R.W., Boella, R.M., Milton, J.A., German, C.R., Bayon, G., Burton, K., 2002. Hf isotope ratio analysis using multi-collector inductively coupled plasma mass spectrometry: an evaluation of isobaric interference corrections. *Journal of Analytical Atomic Spectrometry* 17, 1567–1574.
- Chung, S.L., Lo, C.H., Lee, T.Y., Zhang, Y.Q., Xie, Y.W., Li, X.H., Wang, K.L., Wang, P.L., 1998. Diachronous uplift of the Tibetan plateau starting 40 Myr ago. *Nature* 394, 769–773.
- Chung, S.L., Liu, D.Y., Ji, J.Q., Chu, M.F., Lee, H.Y., Wen, D.J., Lo, C.H., Lee, T.Y., Qian, Q., Zhang, Q., 2003. Adakites from continental collision zones: melting of thickened lower crust beneath southern Tibet. *Geology* 31, 1021–1024.
- Chung, S.-L., Chu, M.-F., Zhang, Y., Xie, Y., Lo, C.-H., Lee, T.-Y., Lan, C.-Y., Li, X., Zhang, Q., Wang, Y., 2005. Tibetan tectonic evolution inferred from spatial and temporal variations in post-collisional magmatism. *Earth-Science Reviews* 68, 173–196.

- Chung, S.-L., Chu, M.-F., Ji, J., O'Reilly, S.Y., Pearson, N.J., Liu, D., Lee, T.-Y., Lo, C.-H., 2009. The nature and timing of crustal thickening in Southern Tibet: geochemical and zircon Hf isotopic constraints from postcollisional adakites. *Tectonophysics* 477, 36–48.
- Chung, S.-L., Wu, F.-Y., Zhao, Z.-D., 2012. The Tibetan orogenic evolution: new advances from pre- to post-collisional geologic records. *Journal of Asian Earth Sciences* 53, 1–2.
- Cooke, D.R., Hollings, P., Walsh, J.L., 2005. Giant porphyry deposits: characteristics, distribution, and tectonic controls. *Economic Geology* 100, 801–818.
- Crawford, A.J., Meffre, S., Squire, R.J., Barron, L.M., Falloon, T.J., 2007. Middle and late Ordovician magmatic evolution of the Macquarie arc, Lachlan Orogen, New South Wales. *Australian Journal of Earth Sciences* 54, 181–214.
- Defant, M.J., Drummond, M.S., 1990. Derivation of some modern arc magmas by melting of young subducted lithosphere. *Nature* 347, 662–665.
- Ding, X., Lundstrom, C., Huang, F., Li, J., Zhang, Z.M., Sun, X.M., Liang, J.L., Sun, W.D., 2009. Natural and experimental constraints on formation of the continental crust based on niobium-tantalum fractionation. *International Geology Review* 51, 473–501.
- Ding, X., Hu, Y.H., Zhang, H., Li, C.Y., Ling, M.X., Sun, W.D., 2013. Major Nb/Ta fractionation recorded in garnet amphibolite facies metagabbro. *Journal of Geology* 121, 255–274.
- Dong, Y.H., Xu, J.F., Zeng, Q.G., Mao, G.Z., Li, J., 2006. Is there a Neo-Tethys' subduction record earlier than arc volcanic rocks in the Sangri group? *Acta Petrologica Sinica* 22, 661–668 (in Chinese with English Abstract).
- Foley, S., Tiepolo, M., Vannucci, R., 2002. Growth of early continental crust controlled by melting of amphibolite in subduction zones. *Nature* 417, 837–840.
- Gao, S.B., Zheng, Y.Y., 2006. Geochemical controlling of mineralization in Qulong super-large porphyry copper deposit. *Tibet. Geological Science and Technology Information* 25, 41–46 (in Chinese with English abstract).
- Gao, Y.F., Hou, Z.Q., Wei, R.H., 2003a. Neogene porphyries from Gangdese: petrological, geochemical characteristics and geodynamic significances. *Acta Petrologica Sinica* 19, 418–428 (in Chinese with English abstract).
- Gao, Y.F., Hou, Z.Q., Wei, R.H., Zhao, R.S., 2003b. Post-collisional adakitic porphyries in Tibet: geochemical and Sr-Nd-Pb isotopic constraints on partial melting of oceanic lithosphere and crust-mantle interaction. *Acta Geologica Sinica English Edition* 77, 194–203.
- Gao, Y., Hou, Z., Kamber, B.S., Wei, R., Meng, X., Zhao, R., 2007a. Lamproitic rocks from a continental collision zone: evidence for recycling of subducted tethyan oceanic sediments in the mantle beneath southern Tibet. *Journal of Petrology* 48, 729–752.
- Gao, Y.F., Hou, Z.Q., Kamber, B.S., Wei, R.H., Meng, X.J., Zhao, R.S., 2007b. Adakite-like porphyries from the southern Tibetan continental collision zones: evidence for slab melt metasomatism. *Contributions to Mineralogy and Petrology* 153, 105–120.
- Gao, Y.F., Wei, R.H., Hou, Z.Q., Tian, S.H., Zhao, R.S., 2008. Eocene high-MgO volcanism in southern Tibet: new constraints for mantle source characteristics and deep processes. *Lithos* 105, 63–72.
- Gao, Y.F., Yang, Z.S., Hou, Z.Q., Wei, R.H., Meng, X.J., Tian, S.H., 2010a. Eocene potassic and ultrapotassic volcanism in south Tibet: new constraints on mantle source characteristics and geodynamic processes. *Lithos* 117, 20–32.
- Gao, Y.F., Yang, Z.S., Santosh, M., Hou, Z.Q., Wei, R.H., Tian, S.H., 2010b. Adakitic rocks from slab melt-modified mantle sources in the continental collision zone of southern Tibet. *Lithos* 119, 651–663.
- Griffin, W.L., Pearson, N.J., Belousova, E., Jackson, S.E., van Achterbergh, E., O'Reilly, S.Y., Shee, S.R., 2000. The Hf isotope composition of cratonic mantle: LAM-MC-ICPMS analysis of zircon megacrysts in kimberlites. *Geochimica et Cosmochimica Acta* 64, 133–147.
- Guo, Z.F., Wilson, M., Liu, J.Q., 2007. Post-collisional adakites in south Tibet: products of partial melting of subduction-modified lower crust. *Lithos* 96, 205–224.
- Hoefs, J., 2009. Stable Isotope Geochemistry, 6th ed. Springer-Verlag, Berlin.
- Hou, Z.Q., Mo, X.X., Gao, Y.F., Qu, X.M., Meng, X.J., 2003. Adakite, a possible host rock for porphyry copper deposits: case studies of porphyry copper belts in Tibet Plateau and in Northern Chile. *Mineral Deposits* 22, 1–12 (in Chinese with English abstract).
- Hou, Z.Q., Gao, Y.F., Meng, X.J., Qu, X.M., Huang, W., 2004a. Genesis of adakitic porphyry and tectonic controls on the Gangdese Miocene porphyry copper belt in the Tibetan orogen. *Acta Petrologica Sinica* 20, 239–248 (in Chinese with English abstract).
- Hou, Z.Q., Gao, Y.F., Qu, X.M., Rui, Z.Y., Mo, X.X., 2004b. Origin of adakitic intrusives generated during mid-Miocene east-west extension in southern Tibet. *Earth and Planetary Science Letters* 220, 139–155.
- Hou, Z.Q., Qu, X.M., Wang, S.X., Du, A.D., Gao, Y.F., Huang, W., 2004c. Re-Os age for molybdenite from the Gangdese porphyry copper belt on Tibetan plateau: Implication for geodynamic setting and duration of the Cu mineralization. *Science in China Series D: Earth Sciences* 47, 221–231 (in Chinese with English abstract).
- Hou, Z.Q., Meng, X.J., Qu, X.M., Gao, Y.F., 2005. Copper ore potential of adakitic intrusives in Gangdese porphyry copper belt: constrains from rock phase and deep melting process. *Mineral Deposits* 24, 108–121 (in Chinese with English abstract).
- Hou, Z.Q., Yang, Z.S., Xu, W.Y., Mo, X.X., Ding, L., Gao, Y.F., Dong, F.L., Li, G.M., Qu, X.M., Li, G.M., Zhao, Z.D., Jiang, S.H., Meng, X.J., Li, Z.Q., Qin, K.Z., Yang, Z.M., 2006. Metallogenesis in Tibetan collisional orogenic belt: I. Mineralization in main-collisional transformation setting. *Mineral Deposits* 25, 337–358 (in Chinese with English abstract).
- Hou, Z.Q., Yang, Z.M., Qu, X.M., Meng, X.J., Li, Z.Q., Beaudoin, G., Rui, Z.Y., Gao, Y.F., Zaw, K., 2009. The Miocene Gangdese porphyry copper belt generated during post-collisional extension in the Tibetan Orogen. *Ore Geology Reviews* 36, 25–51.
- Hou, Z.Q., Zheng, Y.C., Yang, Z.M., Yang, Z.S., 2012. Metallogenesis of continental collision setting: part I: Gangdese Cenozoic porphyry Cu-Mo systems in Tibet. *Mineral Deposits* 31, 647–670 (in Chinese with English abstract).
- Hou, Z.Q., Zheng, Y.C., Yang, Z.M., Rui, Z.Y., Zhao, Z.D., Jiang, S.H., Qu, X.M., Sun, Q.Z., 2013. Contribution of mantle components within juvenile lower-crust to collisional zone porphyry Cu systems in Tibet. *Mineralium Deposita* 48, 173–192.
- Ickert, R., Hiess, J., Williams, I., Holden, P., Ireland, T., Lanc, P., Schram, N., Foster, J., Clement, S., 2008. Determining high precision, in situ, oxygen isotope ratios with a SHRIMP II: analyses of MPI-DING silicate-glass reference materials and zircon from contrasting granites. *Chemical Geology* 257, 114–128.
- Irvine, T.N., Baragar, W.R.A., 1971. A guide to the Chemical Classification of the Common Volcanic Rocks.
- Kay, R.W., 1978. Aleutian magnesian andesites – melts from subducted Pacific ocean crust. *Journal of Volcanology and Geothermal Research* 4, 117–132.
- Le Maitre, R., Bateman, P., Dudek, A., 1989. A Classification of Igneous Rocks and Glossary of Terms. Blackwell, Oxford.
- Li, G.M., Rui, Z.Y., 2004. Diagenetic and mineralization ages for the porphyry copper deposits in the Gangdese metallogenic belt, southern Xizang. *Geotectonica et Metallogenesis* 28, 165–170 (in Chinese with English abstract).
- Li, J.X., Qin, K.Z., Li, G.M., Xiao, B., Chen, L., Zhao, J.X., 2011. Post-collisional ore-bearing adakitic porphyries from Gangdese porphyry copper belt, southern Tibet: melting of thickened juvenile arc lower crust. *Lithos* 126, 265–277.
- Li, C.-Y., Zhang, H., Wang, F.-Y., Liu, J.-Q., Sun, Y.-L., Hao, X.-L., Li, Y.-L., Sun, W., 2012a. The formation of the Daboshan porphyry molybdenum deposit induced by slab rollback. *Lithos* 150, 101–110.
- Li, H., Ling, M.X., Li, C.Y., Zhang, H., Ding, X., Yang, X.Y., Fan, W.M., Li, Y.L., Sun, W.D., 2012b. A-type granite belts of two chemical subgroups in central eastern China: indication of ridge subduction. *Lithos* 150, 26–36.
- Liang, X.R., Wei, G.J., Li, X.H., Liu, Y., 2003. Precise measurement of $^{143}\text{Nd}/^{144}\text{Nd}$ and Sm/Nd ratios using multiple-collectors inductively coupled plasma-mass spectrometer (MC-ICPMS). *Geochimica* 32, 91–96 (in Chinese with English abstract).
- Liang, J.L., Ding, X., Sun, X.M., Zhang, Z.M., Zhang, H., Sun, W.D., 2009. Nb/Ta fractionation observed in eclogites from the Chinese continental scientific drilling project. *Chemical Geology* 268, 27–40.
- Ling, M.X., Wang, F.Y., Ding, X., Hu, Y.H., Zhou, J.B., Zartman, R.E., Yang, X.Y., Sun, W.D., 2009. Cretaceous ridge subduction along the Lower Yangtze River belt, eastern China. *Economic Geology* 104, 303–321.
- Ling, M.X., Wang, F.Y., Ding, X., Zhou, J.B., Sun, W.D., 2011. Different origins of adakites from the Dabie Mountains and the Lower Yangtze River Belt, eastern China: geochemical constraints. *International Geology Review* 53, 727–740.
- Ling, M.X., Li, Y., Ding, X., Teng, F.Z., Yang, X.Y., Fan, W.M., Xu, Y.G., Sun, W.D., 2013a. Destruction of the North China Craton induced by ridge subductions. *Journal of Geology* 121, 197–213.
- Ling, M.X., Liu, Y.L., Williams, I.S., Teng, F.Z., Yang, X.Y., Ding, X., Wei, G.J., Xie, L.H., Deng, W.F., Sun, W.D., 2013b. Formation of the world's largest REE deposit through protracted fluxing of carbonatite by subduction-derived fluids. *Scientific Reports* 3.
- Liu, Y., Liu, H.C., Li, X.H., 1996. Simultaneous and precise determination of 40 trace elements in rock samples using ICP-MS. *Geochimica* 25, 552–558.
- Liu, S.-A., Li, S., He, Y., Huang, F., 2010a. Geochemical contrasts between early Cretaceous ore-bearing and ore-barren high-Mg adakites in central-eastern China: implications for petrogenesis and Cu-Au mineralization. *Geochimica et Cosmochimica Acta* 74, 7160–7178.
- Liu, Y.S., Gao, S., Hu, Z.C., Gao, C.G., Zong, K.Q., Wang, D.B., 2010b. Continental and oceanic crust recycling-induced melt-peridotite interactions in the Trans-North China Orogen: U-Pb dating, Hf isotopes and trace elements in zircons from mantle xenoliths. *Journal of Petrology* 51, 537–571.
- Liu, Y.S., Hu, Z.C., Zong, K.Q., Gao, C.G., Gao, S., Xu, J.A., Chen, H.H., 2010c. Reappraisal and refinement of zircon U-Pb isotope and trace element analyses by LA-ICP-MS. *Chinese Science Bulletin* 55, 1535–1546.
- Liu, D., Zhao, Z., Zhu, D.-C., Niu, Y., DePaolo, D.J., Harrison, T.M., Mo, X., Dong, G., Zhou, S., Sun, C., Zhang, Z., Liu, J., 2014. Postcollisional potassic and ultrapotassic rocks in southern Tibet: mantle and crustal origins in response to India–Asia collision and convergence. *Geochimica et Cosmochimica Acta* 143, 207–231.
- Ludwig, K.R., 2000. User's manual for isoplots/Ex: a geochronological toolkit for Microsoft Excel. Berkeley Geochro-nology Center Special Publication.
- Meng, X.J., Hou, Z.Q., Gao, Y.F., Huang, W., Qu, X.M., Qu, W.J., 2003a. Development of porphyry copper-molybdenum-lead-zinc ore forming system in east Gangdese belt, Tibet: evidence from Re-Os age of molybdenite in Bangpu copper polymetallic deposit. *Mineral Deposits* 22, 246–252 (in Chinese with English abstract).
- Meng, X.J., Hou, Z.Q., Gao, Y.F., Huang, W., Qu, X.M., Qu, W.J., 2003b. Re-Os dating for molybdenite from Qulong porphyry copper deposit in Gangdese metallogenic belt, Xizang and its metallogenic significance. *Geological Review* 49, 660–666 (in Chinese with English abstract).
- Meng, X.J., Hou, Z.Q., Gao, Y.F., Huang, W., 2004. The alteration zoning model of porphyry copper deposit in collisional orogen: case studies of porphyry copper deposits in Gangdese belt, Xizang (Tibet). *Earth Science Frontiers* 11, 201–214 (in Chinese with English abstract).
- Miller, C., Schuster, R., Klotzli, U., Frank, W., Purtscheller, F., 1999. Post-collisional potassic and ultrapotassic magmatism in SW Tibet: geochemical and Sr-Nd-Pb-O isotopic constraints for mantle source characteristics and petrogenesis. *Journal of Petrology* 40, 1399–1424.
- Miller, C., Thoni, M., Frank, W., Schuster, R., Melcher, F., Meisel, T., Zanetti, A., 2003. Geochemistry and tectonomagmatic affinity of the Yungbwa ophiolite, SW Tibet. *Lithos* 66, 155–172.
- Mo, J.H., Liang, H.Y., Yu, H.X., Xie, Y.W., Zhang, Y.Q., 2006. Comparison of ELA-ICP-MS and SHRIMP U-Pb zircon ages of the Chongjiang and Qulong ore-bearing porphyries in the Gangdese porphyry copper belt. *Geotectonica et Metallogenesis* 30, 504–509 (in Chinese with English abstract).
- Mo, X.X., Hou, Z.Q., Niu, Y.L., Dong, G.C., Qu, X.M., Zhao, Z.D., Yang, Z.M., 2007. Mantle contributions to crustal thickening during continental collision: evidence from Cenozoic igneous rocks in southern Tibet. *Lithos* 96, 225–242.
- Mo, X., Niu, Y., Dong, G., Zhao, Z., Zhou, S., Ke, S., 2008. Contribution of syncollisional felsic magmatism to continental crust growth: a case study of the Paleogene Linzizong volcanic succession in southern Tibet. *Chemical Geology* 250, 49–67.

- Molnar, P., 1990. S-Wave residuals from earthquakes in the Tibetan region and lateral variations in the upper mantle. *Earth and Planetary Science Letters* 101, 68–77.
- Molnar, P., Houseman, G.A., Conrad, C.P., 1998. Rayleigh–Taylor instability and convective thinning of mechanically thickened lithosphere: effects of non-linear viscosity decreasing exponentially with depth and of horizontal shortening of the layer. *Geophysical Journal International* 133, 568–584.
- Niu, X.L., Zhao, Z.D., Mo, X.X., Depaolo, D.J., Dong, G., Zhang, S.Q., Zhu, D.C., Guo, T.Y., 2006. Elemental and Sr–Nd–Pb isotopic geochemistry for basic rocks from Decun–Angren ophiolites in Xigaze area, Tibet: implications for the characteristics of the Tethyan upper mantle domain. *Acta Petrologica Sinica* 22, 2875–2888 (in Chinese with English abstract).
- Nomade, S., Renne, P.R., Mo, X.X., Zhao, Z.D., Zhou, S., 2004. Miocene volcanism in the Lhasa block, Tibet: spatial trends and geodynamic implications. *Earth and Planetary Science Letters* 221 (1–4), 227–243.
- Owens, T.J., Zandt, G., 1997. Implications of crustal property variations for models of Tibetan plateau evolution. *Nature* 387, 37–43.
- Oyarzun, R., Marquez, A., Lillo, J., Lopez, I., Rivera, S., 2001. Giant versus small porphyry copper deposits of Cenozoic age in northern Chile: adakitic versus normal calc-alkaline magmatism. *Mineralium Deposita* 36, 794–798.
- Pan, G.T., Mo, X.X., Hou, Z.Q., Zhu, D.C., Wang, L.Q., Li, G.M., Zhao, Z.D., Geng, Q.R., Liao, Z.L., 2006. Spatial-temporal framework of the Gangdese Orogenic Belt and its evolution. *Acta Petrologica Sinica* 22, 521–533 (in Chinese with English abstract).
- Qin, K.Z., Xia, D.X., Li, G.M., Xiao, B., Duo, J., Jiang, G.W., Zhao, J.X., 2014. The Qulong Porphyry–Skarn Copper–Molybdenum Deposit in Tibet. Science Press, Beijing, Chinese.
- Qu, X.M., Hou, Z.Q., Huang, W., 2001. Is Gangdese porphyry copper belt the second “Yulong” copper belt? *Mineral Deposits* 20, 355–366 (in Chinese with English abstract).
- Qu, X.M., Hou, Z.Q., Li, Y.G., 2004. Melt components derived from a subducted slab in late orogenic ore-bearing porphyries in the Gangdese copper belt, southern Tibetan plateau. *Lithos* 74, 131–148.
- Qu, X., Hou, Z., Zaw, K., Youguo, L., 2007. Characteristics and genesis of Gangdese porphyry copper deposits in the southern Tibetan Plateau: preliminary geochemical and geochronological results. *Ore Geology Reviews* 31, 205–223.
- Qu, X.M., Jiang, J.H., Xin, H.B., Chen, H., 2010. A study of two groups of adakite almost simultaneously formed in Gangdese collisional orogen, Tibet: why does one group contain copper mineralization and the other not? *Mineral Deposits* 29, 381–394 (in Chinese with English abstract).
- Rudnick, R.L., Gao, S., 2003. Composition of the continental crust. In: Heinrich, D.H., Turekian, K.K.E. (Eds.), *Treatise on Geochemistry*. Pergamon, Oxford, pp. 1–64.
- Rui, Z.Y., Hou, Z.Q., Qu, X.M., Zhang, L.S., Wang, L.S., Liu, Y.L., 2003. Metallogenetic epoch of Gangdese porphyry copper belt and uplift of Qinghai–Tibet Plateau. *Mineral Deposits* 22, 217–225 (in Chinese with English abstract).
- Sillitoe, R.H., 1997. Characteristics and controls of the largest porphyry copper–gold and epithermal gold deposits in the circum-Pacific region. *Australian Journal of Earth Sciences* 44, 373–388.
- Sillitoe, R.H., 2010. Porphyry copper systems. *Economic Geology* 105, 3–41.
- Soderlund, U., Patchett, J.P., Vervoort, J.D., Isachsen, C.E., 2004. The Lu–176 decay constant determined by Lu–Hf and U–Pb isotope systematics of Precambrian mafic intrusions. *Earth and Planetary Science Letters* 219, 311–324.
- Sun, S.-s., McDonough, W.F., 1989. Chemical and isotopic systematics of oceanic basalts: implications for mantle composition and processes. *Geological Society of London, Special Publication* 42, 313–345.
- Sun, W.D., Ling, M.X., Yang, X.Y., Fan, W.M., Ding, X., Liang, H.Y., 2010. Ridge subduction and porphyry copper–gold mineralization: an overview. *Science China–Earth Sciences* 53, 475–484.
- Sun, W.D., Zhang, H., Ling, M.X., Ding, X., Chung, S.L., Zhou, J.B., Yang, X.Y., Fan, W.M., 2011. The genetic association of adakites and Cu–Au ore deposits. *International Geology Review* 53, 691–703.
- Sun, W.D., Ling, M.X., Chung, S.L., Ding, X., Yang, X.Y., Liang, H.Y., Fan, W.M., Goldfarb, R., Yin, Q.Z., 2012a. Geochemical constraints on adakites of different origins and copper mineralization. *Journal of Geology* 120, 105–120.
- Sun, W.D., Ling, M.X., Ding, X., Chung, S.L., Yang, X.Y., Fan, W.M., 2012b. The genetic association of adakites and Cu–Au ore deposits: a reply. *International Geology Review* 54, 370–372.
- Sun, W.D., Liang, H.Y., Ling, M.X., Zhan, M.Z., Ding, X., Zhang, H., Yang, X.Y., Li, Y.L., Ireland, T.R., Wei, Q.R., Fan, W.M., 2013. The link between reduced porphyry copper deposits and oxidized magmas. *Geochimica et Cosmochimica Acta* 103, 263–275.
- Sun, W., Huang, R.-f., Li, H., Hu, Y.-b., Zhang, C.-c., Sun, S.-j., Zhang, L.-p., Ding, X., Li, C.-y., Zartman, R.E., Ling, M.-x., 2015. Porphyry deposits and oxidized magmas. *Ore Geology Reviews* 65, 97–131.
- Trotter, J.A., Williams, I.S., Barnes, C.R., Lecuyer, C., Nicoll, R.S., 2008. Did cooling oceans trigger Ordovician biodiversification? Evidence from conodont thermometry. *Science* 321, 550–554.
- Tu, X.L., Zhang, H., Deng, W.F., Liang, H.Y., Liu, Y., Sun, W.D., 2011. Application of resolution in-situ laser ablation ICP-MS in trace element analyses. *Geochimica* 40, 83–98 (in Chinese with English abstract).
- Valley, J.W., Lackey, J.S., Cavosie, A.J., Clechenko, C.C., Spicuzza, M.J., Basei, M.A.S., Bindeman, I.N., Ferreira, V.P., Sial, A.N., King, E.M., Peck, W.H., Sinha, A.K., Wei, C.S., 2005. 4.4 billion years of crustal maturation: oxygen isotope ratios of magmatic zircon. *Contributions to Mineralogy and Petrology* 150, 561–580.
- Vidal, P., Cocherie, A., Lefort, P., 1982. Geochemical investigations of the origin of the Manaslu Leucogranite (Himalaya, Nepal). *Geochimica et Cosmochimica Acta* 46, 2279–2292.
- Wang, L.L., Mo, X.X., Li, B., Dong, G.C., Zhao, Z.D., 2006. Geochronology and geochemistry of the ore-bearing porphyry in Qulong Cu (Mo) Ore Deposit, Tibet. *Acta Petrologica Sinica* 22, 1001–1008 (in Chinese with English abstract).
- Wang, B.D., Xu, J.F., Chen, J.L., Zhang, X.G., Wang, L.Q., Xia, B.B., 2010. Petrogenesis and geochronology of the ore-bearing porphyritic rocks in Tangbulu porphyry molybdenum–copper deposit in the eastern segment of the Gangdese metallogenic belt. *Acta Petrologica Sinica* 26, 1820–1832 (in Chinese with English abstract).
- Wang, Z.H., Liu, Y.L., Liu, H.F., Guo, L.S., Zhang, J.S., Xu, K.F., 2012. Geochronology and geochemistry of the Bangpu Mo–Cu porphyry ore deposit, Tibet. *Ore Geology Reviews* 46, 95–105.
- Watson, E.B., Cherniak, D.J., 1997. Oxygen diffusion in zircon. *Earth and Planetary Science Letters* 148, 527–544.
- Wei, G.J., Liang, X.R., Li, X.H., Liu, Y., 2002. Precise measurement of Sr isotopic composition of liquid and solid base using (LP)MC-ICPMS. *Geochimica* 31, 295–299 (in Chinese with English abstract).
- Winchester, J.A., Floyd, P.A., 1977. Geochemical discrimination of different magma series and their differentiation products using immobile elements. *Chemical Geology* 20, 325–343.
- Wu, F.Y., Yang, J.H., 2006. Zircon U–Pb and Hf isotopic constraints on the multiple components in granites. *Geochimica et Cosmochimica Acta* 70, A709–A709.
- Wu, F.Y., Yang, Y.H., Xie, L.W., Yang, J.H., Xu, P., 2006. Hf isotopic compositions of the standard zircons and baddeleyites used in U–Pb geochronology. *Chemical Geology* 234, 105–126.
- Xiao, Y.L., Sun, W.D., Hoefs, J., Simon, K., Zhang, Z.M., Li, S.G., Hofmann, A.W., 2006. Making continental crust through slab melting: constraints from niobium–tantalum fractionation in UHP metamorphic rutile. *Geochimica et Cosmochimica Acta* 70, 4770–4782.
- Xiao, B., Qin, K., Li, G., Li, J., Xia, D., Chen, L., Zhao, J., 2012a. Highly oxidized magma and fluid evolution of Miocene Qulong giant porphyry Cu–Mo deposit, southern Tibet, China. *Resource Geology* 62, 4–18.
- Xiao, B., Qin, K.Z., Li, G.M., Li, J.X., Xia, D.X., Chen, L., Zhao, J.X., 2012b. Highly oxidized magma and fluid evolution of Miocene Qulong giant porphyry Cu–Mo deposit, southern Tibet, China. *Resource Geology* 62, 4–18.
- Xu, J.F., Castillo, P.R., 2004. Geochemical and Nd–Pb isotopic characteristics of the Tethyan asthenosphere: implications for the origin of the Indian Ocean mantle domain. *Tectonophysics* 393, 9–27.
- Xu, W.C., Zhang, H.F., Guo, L., Yuan, H.L., 2010. Miocene high Sr/Y magmatism, south Tibet: product of partial melting of subducted Indian continental crust and its tectonic implication. *Lithos* 114, 293–306.
- Yang, Z.M., 2008. The Qulong giant porphyry copper deposit. Tibet: Magmatism and Mineralization. Chinese Academy of Geological Sciences, Beijing, China, p. 145 (in Chinese with English abstract).
- Yang, Z.M., Hou, Z.Q., 2009. Genesis of giant porphyry Cu deposit at Qulong, Tibet: constraints from Fluid inclusions and H–O isotopes. *Acta Geologica Sinica* 83, 1838–1859 (in Chinese with English abstract).
- Yang, Z.M., Hou, Z.Q., Song, Y.C., Li, Z.Q., Xia, D.X., 2008a. Qulong superlarge porphyry Cu deposit in Tibet: geology, alteration and mineralization. *Mineral Deposits* 27, 279–318 (in Chinese with English abstract).
- Yang, Z.M., Hou, Z.Q., Xia, D.X., Song, Y.C., Li, Z., 2008b. Relationship between Western Porphyry and mineralization in Qulong copper deposit of Tibet and its enlightenment to further exploration. *Mineral Deposits* 27, 28–36 (in Chinese with English abstract).
- Yang, Z.M., Hou, Z.Q., White, N.C., Chang, Z.S., Li, Z.Q., Song, Y.C., 2009. Geology of the post-collisional porphyry copper–molybdenum deposit at Qulong, Tibet. *Ore Geology Reviews* 36, 133–159.
- Yang, Z.M., Hou, Z.Q., Jiang, Y.F., Zhang, H.R., Song, Y.C., 2011. Sr–Nd–Pb and zircon Hf isotopic constraints on petrogenesis of the Late Jurassic granitic porphyry at Qulong, Tibet. *Acta Petrologica Sinica* 27, 2003–2010 (in Chinese with English abstract).
- Yin, A., Harrison, T.M., 2000. Geologic evolution of the Himalayan–Tibetan orogen. *Annual Review of Earth and Planetary Sciences* 28, 211–280.
- Ying, L.J., Wang, D.H., Tang, J.X., Chang, Z.S., Qu, W.J., Zheng, W.B., Wang, H., 2010. Re–Os dating of molybdenite from the Jialma Copper polymetallic deposit in Tibet and its metallogenic significance. *Acta Geologica Sinica* 84, 1165–1174 (in Chinese with English abstract).
- Yogodzinski, G.M., Kay, R.W., Volynets, O.N., Koloskov, A.V., Kay, S.M., 1995. Magnesian andesite in the western Aleutian Kamandorsky region – implications for slab melting and processes in the mantle wedge. *Geological Society of America Bulletin* 107, 505–519.
- Zhang, S.Q., Mahoney, J.J., Mo, X.X., Ghazi, A.M., Milani, L., Crawford, A.J., Guo, T.Y., Zhao, Z.D., 2005. Evidence for a widespread Tethyan upper mantle with Indian–Ocean-type isotopic characteristics. *Journal of Petrology* 46, 829–858.
- Zhao, Z.D., Mo, X.X., Dilek, Y., Niu, Y.L., DePaolo, D.J., Robinson, P., Zhu, D.C., Sun, C.G., Dong, G.C., Zhou, S., Luo, Z.H., Hou, Z.Q., 2009. Geochemical and Sr–Nd–Pb–O isotopic compositions of the post-collisional ultrapotassic magmatism in SW Tibet: petrogenesis and implications for India intra-continental subduction beneath southern Tibet. *Lithos* 113, 190–212.
- Zheng, Y.Y., Xue, Y.X., Cheng, L.J., Fan, Z.H., 2004. Finding, characteristics and significances of Qulong superlarge porphyry copper (molybdenum) deposit, Tibet. *Earth Sciences–Journal of China University of Geosciences* 29, 103–108 (in Chinese with English abstract).
- Zhu, D.C., Zhao, Z.D., Pan, G.T., Lee, H.Y., Kang, Z.Q., Liao, Z.L., Wang, L.Q., Li, G.M., Dong, G.C., Liu, B., 2009. Early cretaceous subduction-related adakite-like rocks of the Gangdese Belt, southern Tibet: products of slab melting and subsequent melt–peridotite interaction? *Journal of Asian Earth Sciences* 34, 298–309.
- Zhu, D.C., Zhao, Z.D., Niu, Y.L., Dilek, Y., Mo, X.X., 2011. Lhasa terrane in southern Tibet came from Australia. *Geology* 39, 727–730.
- Zhu, D.C., Zhao, Z.D., Niu, Y.L., Dilek, Y., Mo, X.X., 2012a. The origin and pre-Cenozoic evolution of the Tibetan Plateau. *Gondwana Research* 23, 1429–1454.
- Zhu, D.-C., Zhao, Z.-D., Niu, Y., Dilek, Y., Wang, Q., Ji, W.-H., Dong, G.-C., Sui, Q.-L., Liu, Y.-S., Yuan, H.-L., Mo, X.-X., 2012b. Cambrian bimodal volcanism in the Lhasa Terrane, southern Tibet: record of an early Paleozoic Andean-type magmatic arc in the Australian proto-Tethyan margin. *Chemical Geology* 328, 290–308.